TRANSMISSION ELECTRON MICROSCOPY CHARACTERIZATIONS WITH *IN SITU* ELECTRICAL MANIPULATIONS ON TWO-DIMENSIONAL MATERIALS

WONG LOK WING

MPhil

The Hong Kong Polytechnic University

2020

The Hong Kong Polytechnic University

Department of Applied Physics

Transmission Electron Microscopy Characterizations with *In Situ* Electrical Manipulations on Two-Dimensional Materials

WONG Lok Wing

A thesis submitted in partial fulfilment of the requirements

for the degree of Master of Philosophy

August 2019

Certificate of Originality

I hereby declare that this thesis is my own work and that, to the best of my knowledge and belief, it reproduces no material previously published or written, nor material that has been accepted for the award of any other degree or diploma, except where due acknowledgement has been made in the text.

_____ (Signature)

___WONG Lok Wing____ (Name of candidate)

Abstract

With nanomaterials emerged since the 1980s, nanotechnology rapidly develops. Recently, two-dimensional materials get enormous attention, which means a van der Waals materials, for example, single-layered graphite, graphene, the first two-dimensional materials. Afterwards, other layered/van der Waals materials have been successfully lowered down to monolayer structure, including h-BN, transition metal dichalcogenides, and Xene (X = Group IV elements). Most of them exhibit excellent properties compared with conventional materials. Thus, the next-generation two-dimensional-based devices are intensively reported. However, there is a lack of fundamental studies in the nano-contact with mechanical and electrical stimulations. In this thesis, transmission electron microscopy characterizations with *in situ* mechanical and electrical manipulations have been conducted. In the nano-contact, the size effect induced electric field is high enough for tunnelling. Field emission dominant transport is preferred, and it has been successfully demonstrated. The corresponding barrier width and height have been statistically analysed in different contact geometry and thickness. All results demonstrated thickness dependence expect for barrier width in face contact. Thickness-dependent electrical conductivity has been studied by current density versus voltage plot and the conductivity is increased with the decreasing thickness. Mechanical force induced screw dislocation has been observed and proved by video record and simulated high-resolution electron microscope image. The slope of the current-voltage plot is almost twice when the screw dislocation is formed, that implies the conductivity is almost double by screw dislocation. Moreover, if the nano-contact is intimately such as welding, the current-voltage usually behaves like thermionic field emission. In terms of mechanical test, titanium

alloy ultrathin film has been bent. The results indicate the grain boundary is the weakest in the whole structure and the flexibility of the film is high. Other than metallic films, wrinkling observations in two-dimensional membranes provide a valuable shape transition and the strain release mechanism. In terms of mechanical-electrical test, stress-dependent electrical properties have been measured. The data demonstrates the tunnelling current and barrier form change with the local stress. These two-dimensional contacts are believed to apply shortly soon. Hence, the *in situ* studies are beneficial to not only the two-dimensional materials fundamental studies, but also the next-generation electronic devices in terms of design, processing, and fabrication. The challenges of two-dimensional devices are stability and feasibility on two-dimensional contacts. The flexibility of two-dimensional materials enhances the tolerance of the contacts. More investigations are needed for forming better two-dimensional contacts in the future.

Acknowledgement

It is a pleasure to thank my supervisor, **Dr. ZHAO Jiong**, for giving me the chance to be one of his students. He provides not only a consistently supportive and stimulating environment in which to study but also generous advice and valuable discussions. Those greatly help my experiments and paperwork. Also, I would like to acknowledge him for teaching the skills of transmission electron microscopy and other related experiments, especially for *in situ* technique.

Thanks for my co-supervisor, **Prof. DAI Jiyan**, for providing suggestions and encouragement.

I am grateful to **Dr. LU Wei**, for teaching basic transmission electron microscopy technique and providing support for transmission electron microscopy centre to ensure transmission electron microscopy runs well.

I want to acknowledge **Dr. LY Thuc Hue** and her group for providing single-layered chemical vapor deposition grown specimen.

Thanks for **Dr. YU Zhiyang** for providing a valuable chance of cooperation to study the metallic crystal that giving me a chance to use *in situ* manipulations to do some mechanical loading to a metallic specimen.

I am appreciative to **ZHENG Fangyuan** and **THI Quoc Huy** for sharing laboratory skills and discussing research questions with me. Thanks for their encouragement, the process of studies get more smoothly.

Thanks for **Deng Qingming** to model the wrinkle shape by the SCC-DFTB.

I am so thankful to **Mr. HO Kai Hong**, for his excellent artisanal skills to make the tiny stages, an add-on for improving *in situ* experiment.

I would also like to thank my colleagues in the Department of Applied Physics and University Research Facility in Materials Characterization and Device Fabrication for discussing, encouraging and helping each other.

Table of Contents

List of Figures

List of Tables

List of Publications

1. Fangyuan Zheng, **Lok Wing Wong**, Quoc Huy Thi, Qingming Deng*, Thuc Hue Ly* and Jiong Zhao*: The critical stable length in wrinkles of two-dimensional materials. Submitted to: ACS Nano. (Associate Editor Assigned)

Chapter 1. Introduction and Literature

This chapter is going to introduce the basis of transmission electron microscopy (TEM) and *in situ* TEM characterization literature. TEM is a powerful tool for us to understand the structure-function relation. In this thesis, mechanical and electrical manipulations inside TEM are focused to investigate different materials properties.

Since the 1980s, fullerene was directly observed in TEM [1] and its spectrum was also recorded [2]. It was a giant step of nanotechnology. Then, carbon nanotube was found in 1991 [3]. The attention on nanotechnology rose and the low-dimensional materials were widely investigated to study their excellent properties and potential applications. Low-dimensional materials are lighter and better functions than conventional materials. For example, carbon fibre provides more strength and less weight than aluminium [4-6]. Recently, carbon fibre reinforced aluminium still gets attention because of low weight and high strength that is promising for the application of sports instruments, aviation, and vehicle [7-9]. On the other hand, the demand for electronic devices keeps rising, and most devices are Si-based integrated circuit. By following Moore's law [10], when the number of transistors can be installed into the chips is doubled with a cycle, the ability of the chips will be also doubled. The cycle was a double per year in the beginning, and then changed to be per a year and a half and became longer. The slowing down has been concerned and it is harder to reduce the scale of the transistor. To keep strengthening the electronic devices, the ability of a transistor is attempting to be upgraded other than only putting more transistor. Then, graphene was firstly exfoliated since 2004 [11]. The scotch tape method and the concept of breaking down van der Waals materials have brainstormed more methods to synthesize two-dimensional (2D) materials, a single-layered van der Waals material [12-15]. Due to the increase of area-to-volume ratio, some fascinating properties of 2D

materials have been discovered such as indirect-to-direct band transition [12-15]. There were several prototypes of transistor made by these new 2D materials with high-performance applications [16-18]. Those applications are promising to fabricate the next-generation electronic devices. To study the functions of the low-dimensional materials, TEM plays an important role to study their structures. The *in situ* manipulations such as heat, force, or/and electricity with TEM characterizations provide more vital information to see how the properties change.

1.1. Introduction

It is essential to understand the functions of the materials by studying structure [19, 20]. TEM is a powerful equipment for us to study the structure of the materials by directly investigating the atomic structure [20]. *In situ* holder enables TEM workers to manipulate specimen inside TEM by force [21-23], electricity [21, 23-27], gas [28-30], and heat [24, 28-33]. Usually, the *in situ* manipulation holder contains two or more features for multipurpose. For instance, catalysis can be conducted by gas flow with the heating holder. Therefore, the direct characterization of structural changes by different stimulations can be observed and recorded. Furthermore, the mechanism of the changes can be investigated more directly to understand the structure-function relation.

Besides, the selected area electron diffraction (SAED) can be recorded to further analyse such as crystal structure and crystallinity. In order to study the atomic structure, the limitation of the resolution is introduced. TEM is different from traditional optical microscopy. The electron beam acts as a light source instead of the photon. The wavelength of the electron (λ_e) is deduced by de Broglie equation and relativistic effects [20] and that of the photon (λ_p) is deduced by Plank-Einstein relation [20, 34],

$$\lambda_e = \frac{h}{\sqrt{2m_e eV\left(1+\frac{eV}{2m_e c^2}\right)}} \quad \textbf{Eq. 1}$$

$$\lambda_p = \frac{hc}{E} \quad \textbf{Eq. 2}$$

where h is the Planck's constant, c is the speed of light, e is the elementary charge, V is the accelerating voltage of the filament, m_e is the rest mass of the electron and E is the energy of the photon. The advantage of using electron beam as a light source is that the theoretical and practical resolution, which is governed by Rayleigh criterion [20],

$$\Delta r_{min} \propto \theta_{min} \propto \frac{\lambda}{D} \quad \textbf{Eq. 3}$$

where Δr_{min} is the minimal resolvable distance, θ_{min} is the minimal resolvable angle, and D is the diameter of the aperture. In comparison between Eq. 1 and Eq. 2, the wavelength generated by electron gun is much shorter than that generated by the photon emission in the same driving voltage. Thus, according to Eq. 3, the minimal resolvable distance or angle of electron source is smaller because of the smaller wavelength. Typically, a wavelength of electron generated by 200 kV electron gun is about 2.5 pA. However, there are limitation and aberrations in the lens system which limits the highest resolution of the TEM. The highest practical resolution in a TEM is denoted by,

$$\Delta r = \sqrt{\Delta r_d^2 + \Delta r_s^2 + \Delta r_c^2} \quad \textbf{Eq. 4}$$

where Δr_d is the diffraction limit, Δr_s is the spherical aberration and Δr_c is the chromatic aberration.

$$\Delta r_d = \frac{0.61\lambda_e}{\sin\beta} \quad \textbf{Eq. 5}$$

$$\Delta r_s = C_s\beta^3 \quad \textbf{Eq. 6}$$

$$\Delta r_c = C_c \frac{\Delta E}{E_0} \beta \qquad \textbf{Eq. 7}$$

where β is the collection semi-angle of the magnifying lens, C_s is the spherical aberration coefficient close to the focal length of lenses, C_c is the chromatic aberration coefficient, ΔE is the energy loss of the electron, and E_0 is the initial beam energy. The diffraction limit can be improved by increasing accelerating voltage to lower the wavelength of the electron or extending the column length of TEM to reduce the collection semi-angle of the magnifying lens. However, increasing accelerating voltage would provide more irradiation damage to the specimen [35-37] and extending the column length of TEM would increase the volume of the TEM chamber which requires a better vacuum system to remain high or ultra-high vacuum level. The effect of spherical aberration and chromatic aberration can be minimized by spherical aberration corrector and monochromator [38]. In this thesis, JEOL 2100F TEM is employed with 200 kV operation voltage.

1.2. Literature of *in situ* TEM characterizations

Since the emerging of low-dimensional materials, their properties are different from bulk because of the change of atomic structure. In terms of low-dimensional materials, graphene and transition metal dichalcogenides (TMDCs) have got enormous attention due to their wide range of applications and special properties. In the perspectives of properties, highly flexible [18, 39, 40], direct-to-indirect band transition [12-15], quantum hall effect [41], piezoelectricity [42, 43], superconductivity [44], supercapacitance [18, 45]. Getting the advantages of their properties, energy storage [18, 45, 46], electronic device [16, 40], gas sensing device [47], photonic devices [48, 49], piezoelectric devices [42], spintronic devices [50], laser [17] and wearable devices [51] have been reported, and some of them with high-performance

compared with the conventional materials [16-18, 42, 48]. However, there is lack of fundamental studies in the nano-contact about the low-dimensional materials. It is critical for lowering down the size of the device. To deal with this, TEM characterizations with *in situ* manipulations would be implemented. The structure-function relations can be studied under TEM and there are several studies about low-dimensional materials by using *in situ* technique in the following. It is beneficial to unravel the behaviour change of the low-dimensional materials by different stimulations. On the other hand, the limitations of 2D materials studies will be also cited below.

As Huang *et. al.* [21] indicated, the superplastic deformation of single-walled carbon nanotube in the high temperature reached 280% which is much greater than the theoretical limit and the thickness is one-fifteenth from the original. This result was conducted by *in situ* TEM pulling test. Although it is well-known that the properties of materials would be different when the size is narrowed down to nanoscale and the temperature is high, the result is indeed surprising for such a dramatic change in plasticity. The heat, approximately 2000 ^{o}C, on the carbon nanotube was generated by a 2.3 V d.c. voltage due to the Joule heating effect. The voltage was applied by external add-on of the *in situ* holder. In situ TEM is a dynamic technique which allows researchers to explore the material science.

In Zhao's [24] studies, *in situ* conductive atomic force microscopy experiment on single crystalline GaN and Ag nanowires was conducted. They found that the model of the breakdown rule for nanowires. Metal nanowires follow electro-breakdown while semiconductor nanowires follow thermo-breakdown because of thermal conductivity and electrical conductivity. Metal nanowires have higher thermal and electrical conductivity. When the high bias voltage is applied over the metal nanowires, the electromigration effect is dominant and the Joule heating effect is negligible. As a result, the metal nanowires

were broken around two ends under a giant voltage. On the contrary, the Joule heating effect on semiconductor nanowires in breakdown mechanism is dominant. It is caused by lower electrical and thermal conductivity. The heat accumulates in the middle of the nanowires and hence it is broken.

Cold welding of ultrathin metal nanowires was observed [22]. Gold and silver nanowires can be welded without any heating and biasing in nanoscale. The welding just needs two nanowires to contact together in an ultrahigh vacuum atmosphere. The welded nanowires had the same conductivity, strength and crystal orientation.

In situ TEM characterization can be also conducted by electron beam irradiation. The electron beam irradiation would provide heating effect, knock-on damage and irradiation damage which would change the structure of materials and the special ability of nano-materials can be investigated in real-time. For instance, elastic-plastic deformation of Si nanowires could be triggered by electron beam irradiation under low strain rate [52]. Amorphization would be induced under high magnification electron beam illumination and the irradiated part would be softened, weakened and extended. As a consequence, the bending strain of Si nanowires achieved over 40%. The second example is that a rigid and stable atomic carbon chain was constructed by gradually irradiating graphene and which was theoretically proved [53]. Phase transformation of 2H-$MoTe_2$ was verified by electron beam irradiation in scanning transmission electron microscopy (STEM) [54]. Te atoms were predicted to be sublimed at about 400 ^{o}C. The heating effect of electron beam irradiation created irreversible Te vacancies such that 2H-$MoTe_2$-to-1T'-$MoTe_2$ transition occurs.

Ni nanowire/multi-wall carbon nanotube/amorphous-carbon nanotube heterojunctions and zinc oxide nanowire have been characterized by *in situ* experiment [25, 26].

The semiconductive nanowires were contacted with a metal probe. The electrical transport mechanisms of the semiconductive nanowires were proposed to be thermionic emission or thermionic field emission within 10 V in metal-semiconductor.

In the perspectives of limitations, although there are many studies about electrical properties of 2D membranes, only a few transistor-based reports highlighted the contact geometric effects on 2D materials [55-58]. On the other hand, field emission is preferred to be the transport regime in M-S nano-contact rather than thermionic emission [25] or thermionic field emission [26] due to the size effect enhanced giant electric field on both W probe and the edge of 2D materials [59]. Besides, metal-semiconductor contact in few nm-scale is absent in the fundamental studies.

In terms of mechanical tests, other than the static flexural testing, the dynamical methods that are feasible with nanowires or nanotubes [60, 61] but unsuitable for atomic membranes due to lack of self-supporting. Alternatively, some ultra-flexible films, such as biofilms [62], were measured by atomic bulging methods [63] or atomic force spectroscopy [64] for experimental evaluation of flexural behaviour. 2D materials such as graphene and single-layer MoS_2 [11, 65, 66], their flexural properties were mainly evaluated theoretically, for example, density functional theory (DFT) calculation [67]. Compared to the basal plane tensile tests available for 2D materials [68], although their nature of high flexibility has been well known, especially based on the facts that nm-diameter nanotubes can be rolled up by the 2D membranes [69, 70] as well as numerous other folded [71] or creased [72] 2D structures have been observed, at present a continuous flexural test on the 2D membranes is still absent, in part due to the difficulties in loading fixture and atomic-scale manipulations on the membranes.

In short summary, TEM characterizations can provide valuable information for understanding the structure-function relations. *In situ* manipulations provide a platform in TEM to observe the structural changes and hence the function changes. At the end, more functions of low-dimensional materials can be discovered and understood.

1.3. Objectives

In this thesis, Nanofactory^{TM} *in situ* scanning tunnelling microscopy-transmission electron microscopy (STM-TEM) holder was employed in all characterization experiments. The low-dimensional materials such as graphene and TMDCs were manipulated by either mechanical or/and electrical stimulation to investigate the structure-function relation. Indeed, although there are many possible applications have been reported above, the mechanism of transport and the mechanical, as well as electrical properties in the nano-contact, are not fully understood. Herein, there are several objectives in this thesis. (1) To study and understand the transport mechanism of metal-semiconductor (M-S) nano-contact which essentially affects the performance of the next-generation instruments and hence to improve their performance effectively. (2) To explore the mechanical properties of 2D membranes. (3) To investigate the thickness-dependent electrical properties. (4) To trigger, monitor and characterize phase transition or defects in the low-dimensional materials. In order to complete the purposes, there are several theories that should be mentioned.

1.4. Basic Theory of Metal-Semiconductor Contact

The formation of metal-semiconductor contact depends on the mismatch of the Fermi level difference between metal and semiconductor. The Fermi level (E_F) is simply equal to the work functions (Φ), which is the minimum energy required for an electron to

exit from a solid to vacuum level. The electron affinity (χ) is the minimum energy required for an electron escapes from conduction band minimum (E_C) to vacuum. The bandgap (E_g) is the gap between the valence band maximum (E_V) to E_C. Once metal contacts with a semiconductor, the E_F of metal and semiconductor would align with each other, that changes the band structure. Using n-type semiconductor as an example **Figure 1**, after contact, if $\Phi_{Metal} > \Phi_{n-type\ Semiconductor}$, a potential barrier ϕ_B would be formed. The current-voltage (I-V) characteristic behaves rectifying. On the contrary, it behaves ohmic and the potential barrier is absent. The behaviour in a p-type semiconductor is reverse under the same condition. The I-V characteristic is important data for analysing the transport regime.

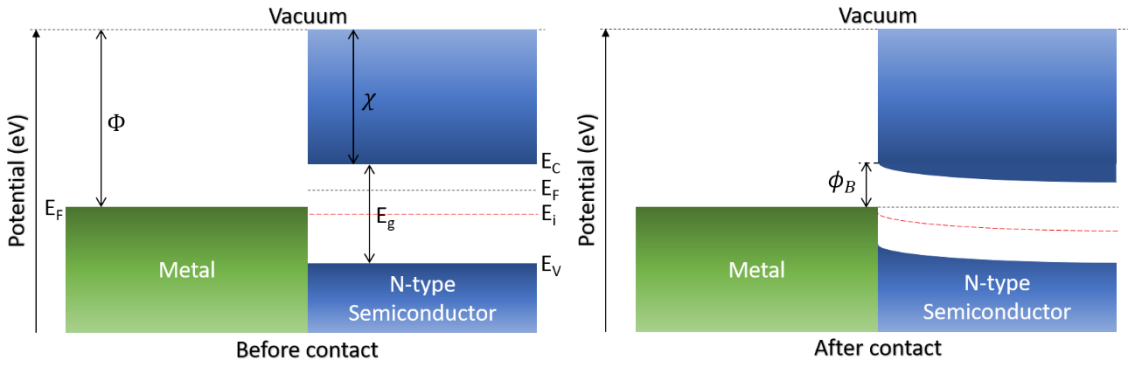

Figure 1 Band structures of metal-semiconductor contact before and after contact.

1.5. Basic Theory of Fowler-Nordheim Tunnelling

There are three main theories of I-V characteristics, including thermionic emission (TE), thermionic field emission (TFE) and field emission (FE). At absolute zero, electron transport completely follows FE. Otherwise, FE, TFE, and TE are coexisted. Under a small electric field, TE is dominant in transport. As the increasing electric field, the contribution of TFE gets more. Under a giant electric field, the effect of FE becomes dominant. In the nano-contact experiment, the STM probe and 2D membranes have very sharp edges. The charge concentration at the edges is higher because of the shape and size

effect. As a result, the electric field across the nano-contact should be huge such that FE is preferred. Fowler-Nordheim (F-N) tunnelling model is a cold FE, which model basically applies when the electric field is greater than 10^8 V/m [73]. This giant field-induced emission of electrons can be emitted from either a solid or liquid. F-N model can be applied for investigating the I-V characteristic of nano-contact. The F-N model is denoted by,

$$I = \frac{aAV^2}{\lambda t^2 \phi} \exp\left(-\frac{\nu b \phi^{\frac{3}{2}} t}{V}\right) \quad \textbf{Eq. 8}$$

where, a is the first F-N constant, b is the second F-N constant, A is the contact area, V is the bias voltage, t is the thickness, ϕ is the potential barrier, λ is the local pre-exponential correction factor which corrects the process of emission, ν is the correction factor for Schottky-Nordheim barrier which is about the shape of the barrier. The model in logarithmic form is easier to be analysed.

$$\ln\left(\frac{I}{V^2}\right) = \ln\left(\frac{aA}{\lambda t^2 \phi}\right) - \frac{\nu b \phi^{\frac{3}{2}} t}{V} = C_1 - \frac{C_2}{V} \quad \textbf{Eq. 9}$$

where C_1 and C_2 are the fitting parameters. The potential barrier and barrier width can be derived from the fitting parameters.

$$\phi^2 = \frac{C_2}{b\nu\sqrt{\frac{e^{C_1}}{\lambda A a}}} \quad \textbf{Eq. 10}$$

$$t^4 = C_2 \times \frac{\left(\frac{e^{C_1}}{\lambda A a}\right)^{\frac{3}{2}}}{b\nu} \quad \textbf{Eq. 11}$$

Since the barrier width depends on permittivity (ε_r), built-in potential (V) and carrier concentration (N_D and N_A), the thickness-dependent permittivity be also estimated [74],

$$t \approx \left[\frac{2\varepsilon_r\varepsilon_0}{q}\left(\frac{1}{N_A}+\frac{1}{N_D}\right)(V_{bi}-V)\right]^{\frac{1}{2}} \quad \textbf{Eq. 12}$$

Chapter 2. Methodology

This chapter is going to introduce the probe preparation, specimen synthesis, setting of TEM, and the electrical and mechanical test with their analytical procedures. Part of the information in Chapter 1 involves in this chapter. The methods we used would be introduced as detailed as possible.

2.1. Tungsten Probe Preparation

An electrochemical method of fabricating tungsten probe was employed in this thesis [75]. The probe was utilized to manipulate the low-dimensional materials either mechanical force or electrical bias. The setup can be seen in **Figure 2**. 3 mm diameter tungsten wire was held and immersed in a droplet of 1 M NaOH solution, which is an etchant, held by a stainless steel plate with a small hole. The tungsten wire was connected to anode and the steel plant was connected to cathode. 6.0 V bias voltage is applied in this system until a tip is dropped. After the tip drops, it will be rinsed by ethanol and deionized water immediately. Finally, the tip is dried by air blower or heat to remove residual liquid on the tip.

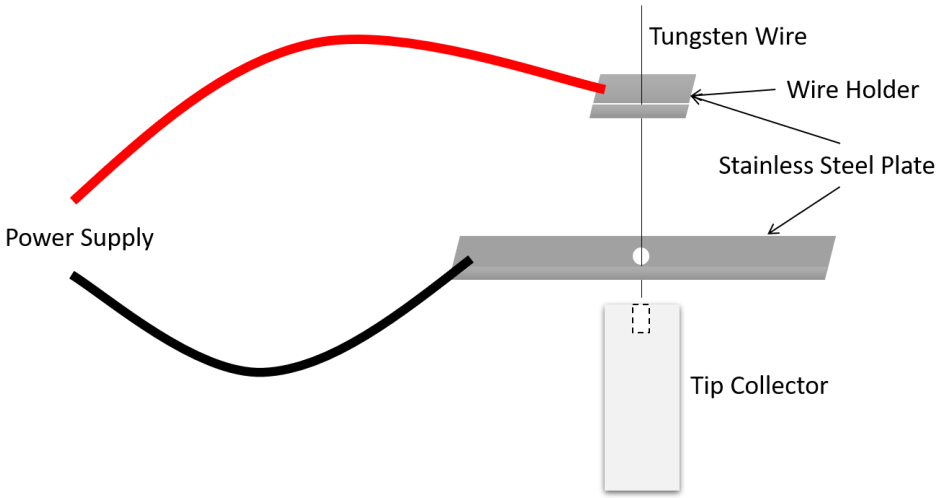

Figure 2 Illustration of the setup of electrochemical etching.

2.2. Specimen Preparation

Specimen preparation for *in situ* TEM characterization can be divided into two categories: bottom-up and top-down. Bottom-up means a specimen is built from the lowest units, atoms. The atoms are arranged properly to react and stack onto each other. Similar to Lego, a Lego building is constructed by numerous small pieces of Lego. Based on this concept, chemical vapour deposition (CVD) and molecular beam epitaxy (MBE) were designed to synthesize low-dimensional materials by precise atom arrangement [76]. Top-down means breaking something big down into small pieces. There are two common top-down approaches which are mechanical exfoliation (ME) and liquid exfoliation (LE). ME and LE are always employed to break down bulk layered materials such as graphite and transition metal dichalcogenides. In the following, four commonly used synthesis strategies will be briefly introduced one by one.

CVD synthesizes materials on a substrate by one or more vaporized precursors in the vacuum. The deposition is taken place on the surface of the substrate by the reaction and/or decomposition of the precursors. Usually, one or more by-products are synthesized simultaneously, but those by-products would be removed by gas flow. The control of the parameters such as ratio of precursors [77], substrate size [77], substrate distance [78], different substrates [79], temperature [80, 81], gas flow rate [80] would totally change the quality of the product.

MBE requires a high vacuum environment (at least 10^{-8} Torr). Pure elements are heated separately until the elements start slowly sublime. The gaseous elements are directly deposited onto a substrate. The elements would react to each other on the substrate. The rate of material impinging on the substrate surface is controlled by the temperature that is a crucial parameter for MBE [76, 82].

ME breaks layered materials down by using a mechanical method. The mechanical force overcomes the van der Waals attraction between adjacent layers. The first ME of graphene by using scotch tape was in 2004 [11]. A graphite was repeatedly exfoliated, and the thickness was gradually reduced until it became single-layered graphite, graphene. There are other ME methods such as ball milling [83, 84] which enhanced the productivity of the ME.

Similar strategy to ME, LE overcomes the van der Waals attraction mainly by sonicating a solution [85-88]. A suitable solvent is necessary for ion intercalation and ion exchange can weaken interlayer van der Waals attraction. The solvent also can avoid reaggregation of the exfoliated materials. Otherwise, the solute will be reaggregated and sedimented.

In this thesis, ME and CVD specimen are involved for both mechanical and electrical measurements. A bulk MoS_2 and highly ordered pyrolytic graphite (ZYA Grade, provided by 2D Semiconductor Inc.) were mechanically exfoliated by conventional scotch tape method [11]. The exfoliated specimen would be transferred by thermal release tape onto conductive TEM grid directly [89]. Then, the thermal release tape can be completely peeled off at 140 ^{o}C. CVD grown MoS_2 and ReS_2 were provided by Dr. LY Thuc Hue and her group.

2.3. Transmission Electron Microscopy Configurations

Since there are contact geometric effect, two main types of contact would be shown in this thesis, which are edge contact and face contact. There are three side view illustration are shown to provide a better understanding of the TEM images in Results

session **Figure 3a-c**. The plane surfaces of the 2D membranes can be perpendicular (planar view) **Figure 3a-b** or parallel (edge-on view, edges were bended) to the viewing direction of TEM. The W probe was gently moved and connected with the edges or surfaces for the two types of contacts. For contacts in planar view, the thickness (layer number) of contact position was confirmed by mechanically bending the edges into edge-on configuration, thus the layer numbers can be directly counted.

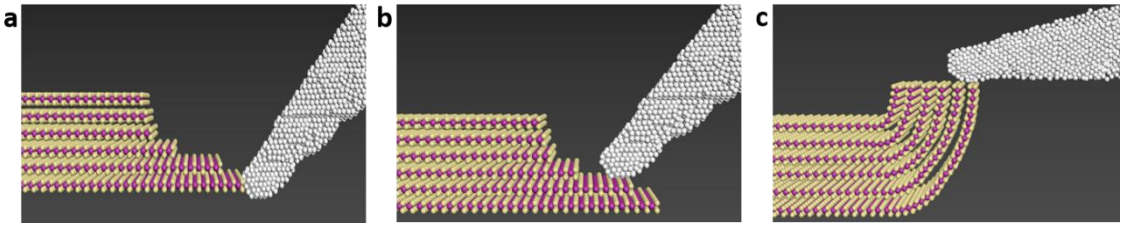

Figure 3 Side view illustrations of **a** 1L MoS_2 edge contact, **b** 2L MoS_2 face contact and **c** 2L MoS_2 edge contact in edge-on configuration. The yellow, purple and white balls on represent Sulfur atoms, Molybdenum atoms and Tungsten atoms, respectively.

2.4. Current-Voltage Measurement

TEM grid was held on the fixed end of Nanofactory *in situ* STM-TEM holder with 15^{o} inclination and W probe was held on a 3-axis controllable hat as seen in **Figure 4**. When the desired flake was observed, the probe would be firstly moved by the inertial slider-driven coarse control. The inertial slider-driven coarse control aims to approach the low-dimensional flake as close as possible such that the flake can be contacted in the fine control range. The piezo-driven fine control has the finest step of 2 pm with the maximum range of ±14.000 μm for up-down and left-right, and ±700.000 nm for forward-backward, allows accurate control to contact with the flake. Then, the I-V measurement can be conducted by using our homemade LabVIEW program.

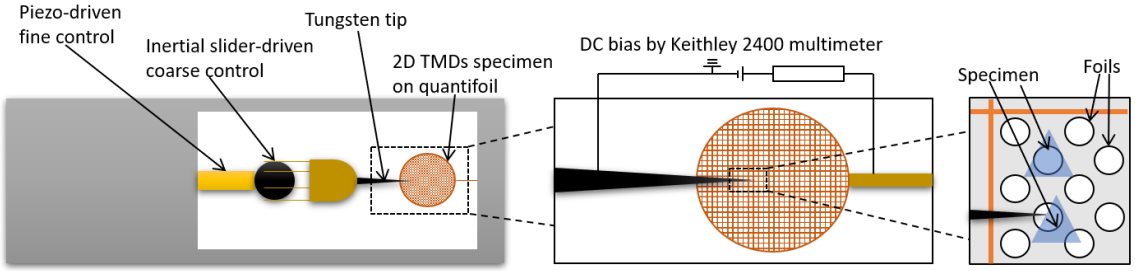

Figure 4 Schematic diagram of *in situ* experiment.

The LabVIEW program was designed for controlling Keithley 2400 to apply bias voltage and measure current flow **Figure 5**. Parameters can be changed such as bias voltage range, pulse voltage steps, increment. After the W probe contacts with a low-dimensional material, the program can be started immediately. The data will be collected in txt file into the destination you set with a file name. The graph in the program can have a quick preview of the I-V measurement.

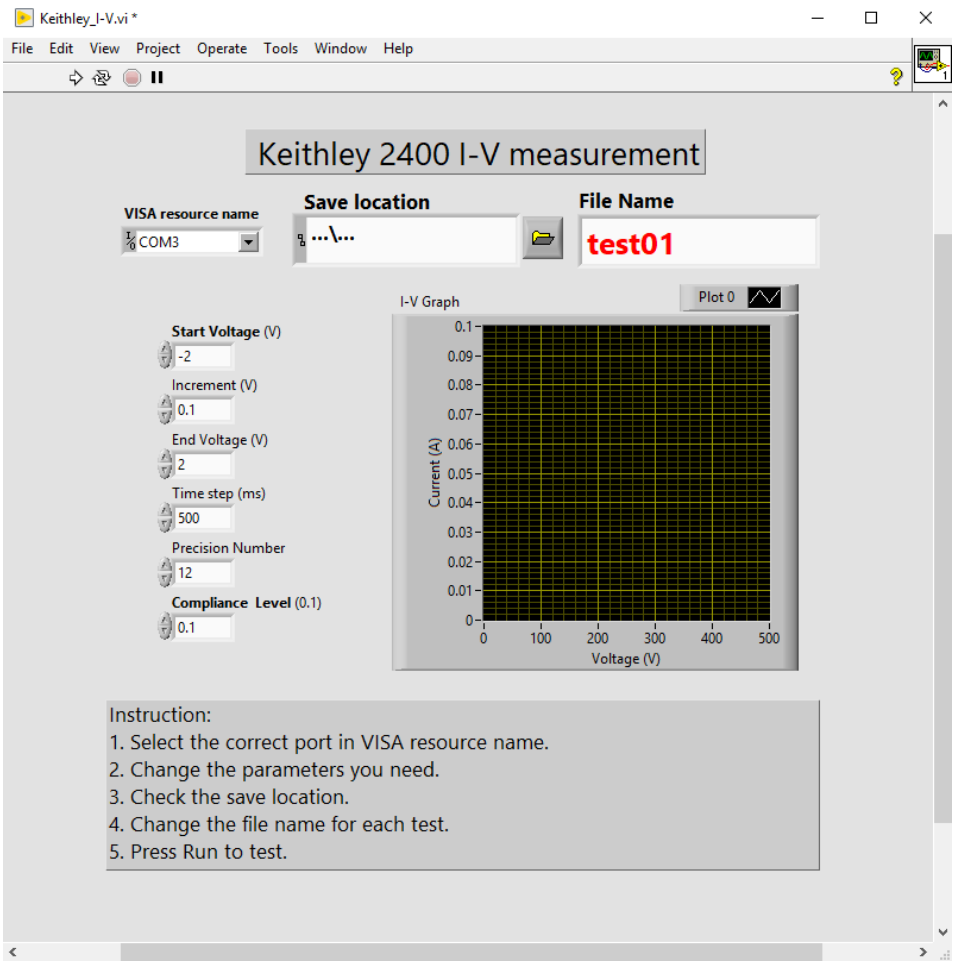

Figure 5 User interface of the homemade LabVIEW Program.

A piezo-controlled sharp W probe was used to manipulate the contacts with the 2D membrane in terms of different thickness, contact configurations, defect types, and stress. The contact area formed were all less than 50 nm^2, and more importantly, one side of the contact was truly in 2D. Different from the bulk or nanowire contacts mentioned above [25, 26, 74], we predicted the field emission (FE) in such 2D contacts was dominant because giant electric field could be built up at the contacts due to the reduced dimension, even in low bias regime (<1.00 V). This can be verified by the F-N plot (**Chapter 1.5**).

2.5. High-Resolution TEM Images Simulation by Multislice in jems

Multislice algorithm is a common method for simulating HRTEM images based on calculating the interaction between electron beam and specimen such as scattering [90]. The condition of the simulation was selected as follow. JEOL 2100F TEM was selected and the preset values were directly used. Specimen setting was along [010] direction. In the HREM map, only defocus, image dup-y and noise were changed to 80.0 min/nm, 6 and 5%, respectively.

2.6. *In Situ* Welding Experiment

2D electrical contacts have been determined to test with different metal probe. The setup was similar to **Chapter 2.4**. The specimen was changed from a grip to a wire as seen in **Figure 6**. Metal nanowires had been attached to the gold wire by rub. The W probe would approach to the metal nanowires which pointed to the desired direction, parallel to the W probe. The aim of this welding experiment is to weld a single nanowire onto the W probe with the same direction. Afterwards, the welded metal nanowire as a probe would contact the 2D materials for the electrical measurements. Different metals

have different work functions. This is a good chance to study 2D electrical contacts with different band formations.

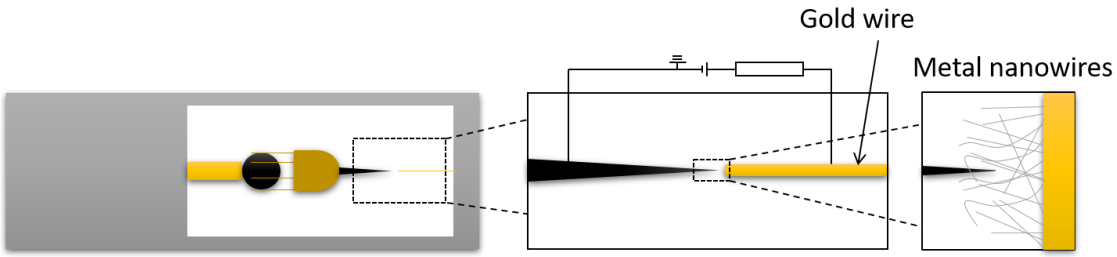

Figure 6 Setup of welding experiment.

2.7. Joule Heating Estimation

The hottest point must be the narrowest cross-session area, where is the M-S nano-contact. Thus, only voltage drop across the M-S nano-contact had to be considered,

$$V_j = V - I_{system}R_{system} \quad \textbf{Eq. 13}$$

The heat would flow through both W probe and 2D membrane. The heat flow of W probe is negligible in this experiment. The estimation can be simplified to assume the electrical conductivity (σ) and thermal conductivity (κ) of the whole 2D membrane are constant. The lowest temperature (T_0) in this system should be at the boundary of the 2D membrane supported by quantifoil and that is approximately equals to room temperature. Consequently, the maximum temperature is [24],

$$T_{max} - T_0 = \frac{\sigma V_j^2}{8\kappa} \quad \textbf{Eq. 14}$$

2.8. Crystal Plane Study Metallic Membrane by Loading Test

Metallic ultrathin films were prepared by Focused Ion Beam (FIB). The specimens were prepared by **Dr. YU**'s group or purchasing from Sandvik™ (SDK). The desired crystal planes were selected and cut to be an ultrathin film. The film was studied by

the mechanical loading test to investigate the mechanical properties of each crystal plane. A schematic diagram can be seen in **Figure 7**. Since the ultrathin film are usually flexible, the loading aims to bend the film until a crack is observed. The cracked specimen would be further analysed by **Dr. YU** by using double Cs-corrected TEM.

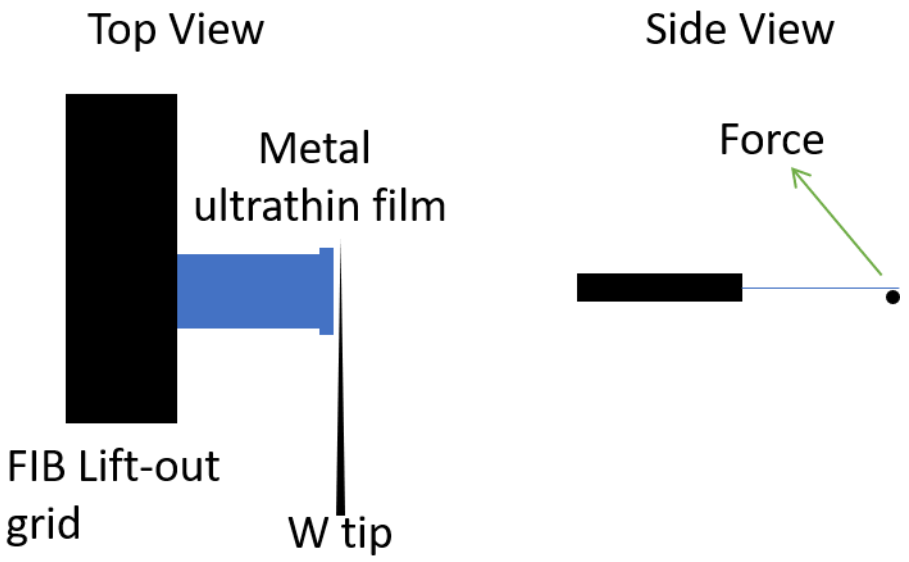

Figure 7 Scheme of loading test from top view and side view.

Chapter 3. Results

Geometric effect of nanoscale contacts was intensively studied by transistor, the electrical transport through the heterojunction between a nanowire or a nanotube is distinct from the bulks [55-58]. Luo *et al.* [25] conducted conductive atomic force microscopy (CAFM) experiment on Ni nanowire/multi-wall carbon nanotube/amorphous-carbon nanotube heterojunctions, and Zhang *et al.* [26] studied the zinc oxide nanowire contacts. They proposed the transport behaviour follows either thermionic emission (TE) or thermionic field emission (TFE) in metal-semiconductor nano-contacts [25, 26]. It should be noted that the size effect [59] is crucial to control the electric field across the junctions, and hence the resultant transport regimes should be FE. Nevertheless, the electrical transport across metal-semiconductor junctions in few nm-scale or less are yet to be fully understood.

We investigated the electrical transport across various types of contacts of 2D MoS_2. The specimen preparations were shown in **Chapter 2.2**. *In situ* TEM-STM technique is a direct method to study the structure-property relationship and empower the atomic-scale understanding of the electrical performances of materials [21, 24]. **Figure 4** shows the experimental schematic of our *in situ* TEM-STM setup, with programmable bias voltage and current measurement module (**Chapter 2.4**). The electrical properties would be measured by I-V data and which would be further analysed.

3.1. Thickness-dependent Conductivity

The thickness-dependent band structure of 2D materials has been widely reported [91-93]. It is interesting to study the conductivity of 2D materials for future nano-devices. TEM images captured from the video are shown in **Figure 8a-d** and **Figure 9a-c**. The

false colour enhanced the thickness contrast in **Figure 8a** and **Figure 9a**, presenting the stair-like structure of the 6-vdW-layered (6L) MoS_2 which enabled the W probe contact different number of vdW layer(s) by changing the contact positions, including the single-layer (1L) contact. **Figure 8a-b** shows a typical 1L edge contact, **Figure 8c-d** display the bilayer (2L) and 6L edge contact, and the 1L, 2L and 6L face contact are shown in **Figure 9a-c**, respectively. The W probe was sufficiently sharp which provided atomic-accurate contact. The 2D (x-y plane) projection effect of TEM may cause overlap between W probe and 2D membranes, however all the edge and face contacts in our experiments have been precisely controlled in three dimension by the movable W probe so that the relative position (including z-direction) of the W probe and membrane edge can be unambiguously determined (**Supplementary video 1** for details). For example, in the video, the probe was moved to the left and then touched a MoS_2 membrane, which was bended into be edge-on configuration, that means face contact is formed. If the probe was moved slightly rightward and let the edge of the flake contact with the W probe, that contact would become edge contact. Simultaneously, the two-terminal I-V measurement for each contact was carried out. The recorded I-V responses showed large variations for different contacts even at the same edge position of the same MoS_2 membrane, exhibiting the contact governed transport behaviour. The electrical conductivities were usually higher for the contacts with a smaller number of layers, irrespective of edge contact or face contact (**Figure 8e** and **Figure 9d**).

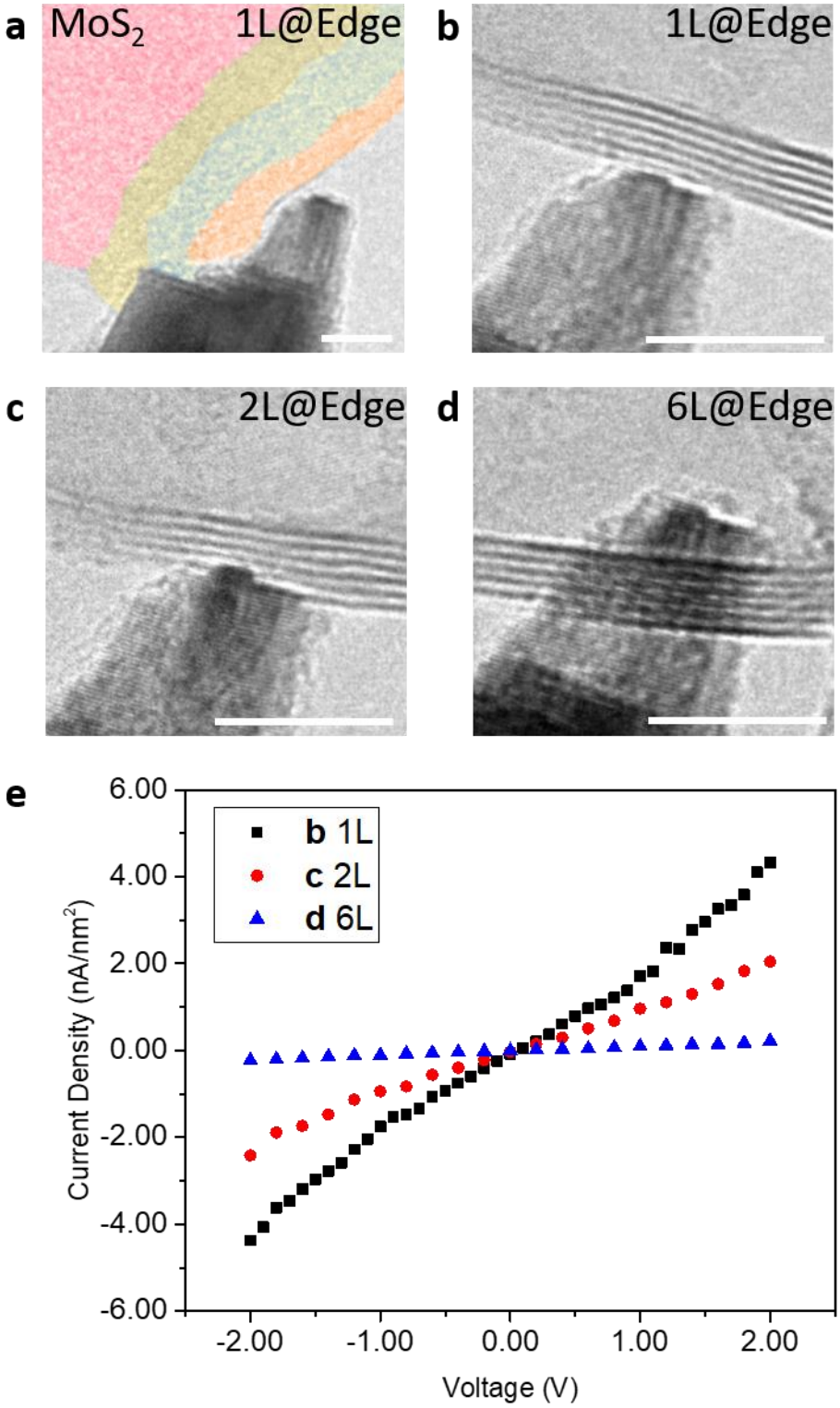

Figure 8 TEM images of (**a**&**b**) 1L, **c** 2L, and **d** 6L edge contact. Scale bar: 5 nm. The colour on **a** aims to enhance the contrast of the stair-like structure. **e** current density versus voltage curve for edge contact.

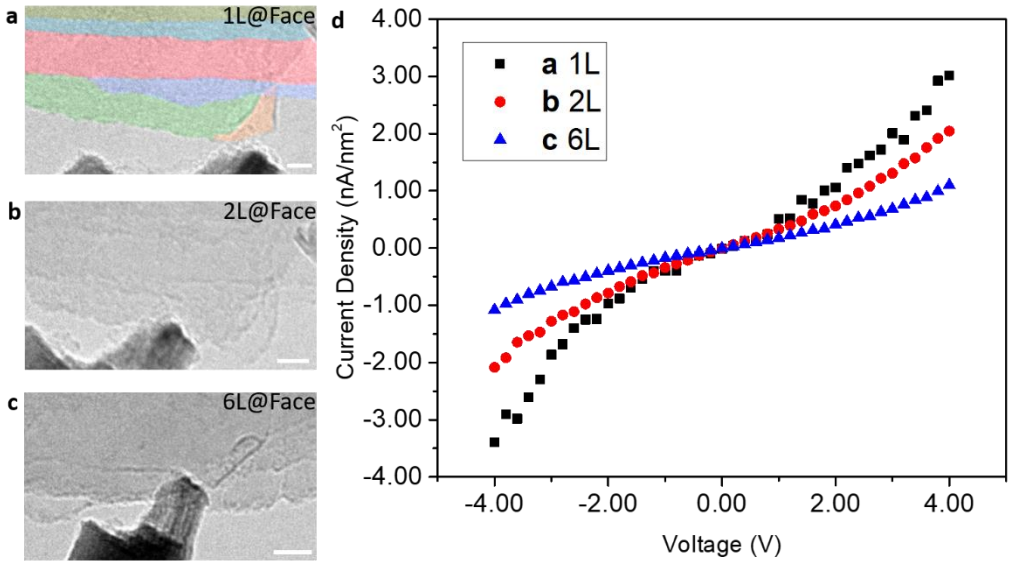

Figure 9 TEM images of **a** 1L, **b** 2L, and **c** 6L edge contact. Scale bar: 5 nm. The colour on **a** aims to enhance the contrast of the stair-like structure. **d** current density versus voltage curve for face contact.

3.2. Thickness and Contact Geometry Effect on Potential Barrier and Barrier Width

Further analysing the I-V data, in most of cases, the I-V behaviour were linear beyond ±2.00 V bias mainly corresponding to the system and MoS_2 specimen (including the edge towards the contact) resistances, and non-linear within ±2.00 V (**Figure 10**) caused by the contact rectification and emission. Therefore, the I-V responses of the contacts within ±2.00 V can be retrieved after subtracting the linear voltage drops contributed by system and sample resistances (**Eq. 13**). Then, the common TE, TFE models for metal-semiconductor contacts were unsuitable for this highly symmetric I-V data (**Figure 11**). TE presents a rectifying I-V behaviour and the I-V behaviour of TFE likes a diode. The best fitting for the measured 2D contact behaviour was the FE, F-N model [94] (**Figure 10** and **Figure 11**). The contact area depends on the probe size which is crucial to the transport regime. FE is dominant on both forward bias and reverse bias when the probe

is within around 10 nm. Furthermore, the potential barrier and barrier width can be determined by the fitted parameters (**Chapter 1.5**). The fitted parameters of all our measured contacts were presented in **Table 1**.

A total number of 21 tests for edge contact and 20 tests for face contact were conducted. The electrical transport showed high reproducibility for each contact type. The potential barriers ranged from 0.042 eV to 0.95 eV and it was found that the potential barrier was smaller when the layer number (thickness) of the contact was smaller (**Figure 12**). Meanwhile, the face contact always had a larger barrier than edge contact for the 1L and 2L contacts. The average potential barriers of edge contact were 0.16 eV, 0.51 eV, and 0.84 eV and the mean of face contact were 0.22 eV, 0.61 eV and 0.72 eV for 1L, 2L, and 6L MoS_2 respectively. The thickness-dependent barrier heights in forward and reverse bias were similar. Although both edge and face contact had increasing barrier heights with the thickness increase, the increasing rate of face contact was less than that of edge contact. As for the barrier width, the results of edge contact decreased with the increase of thickness (**Figure 13**). However, the face contact barrier widths were much smaller and showed thickness independence (**Figure 13**). Besides, all of the barrier width is under 5 Å, which means the barrier is extremely thin. It is beneficial to the tunnelling effect.

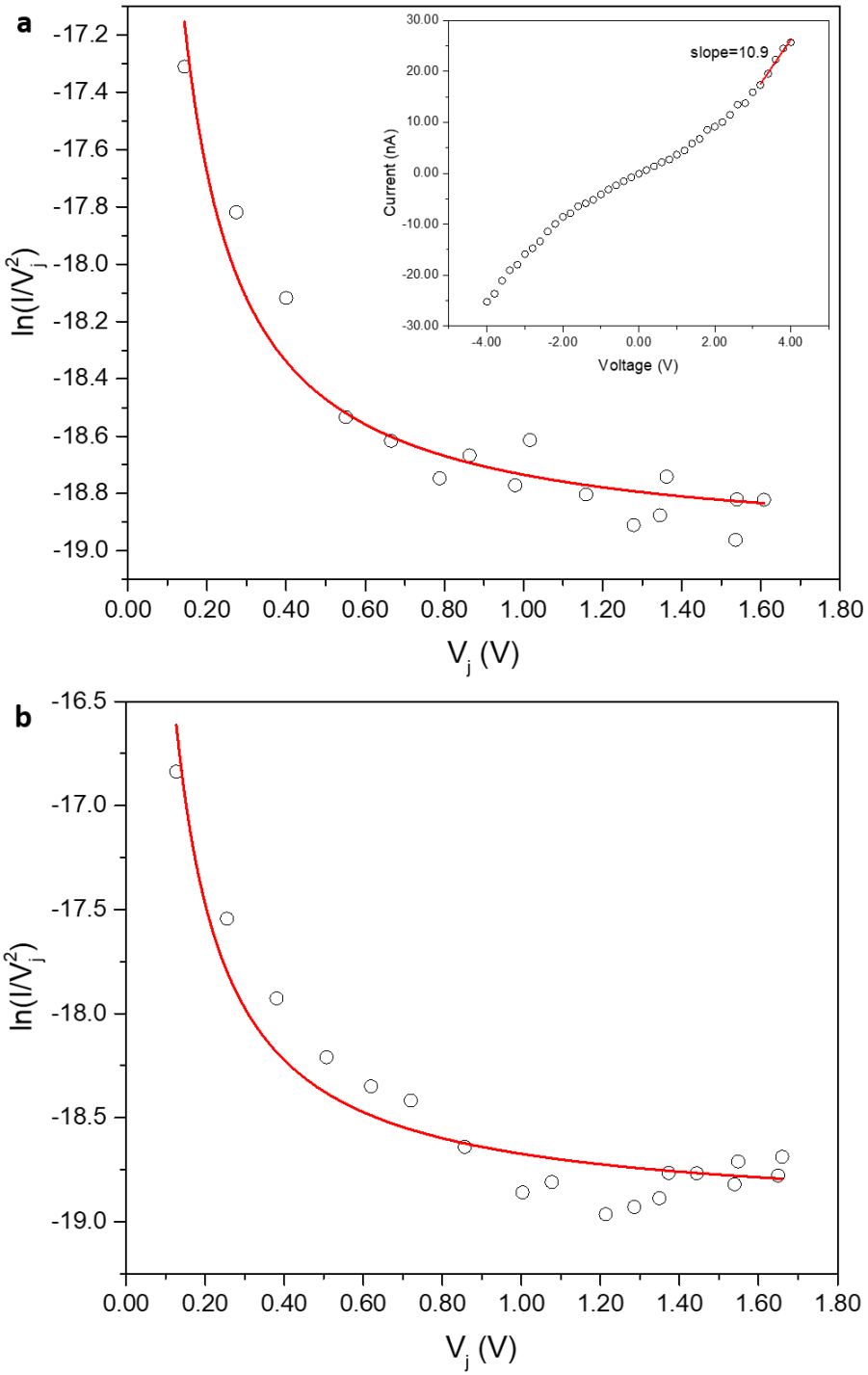

Figure 10 Best Fowler-Nordheim fit with adjusted data in **a** reverse bias and **b** forward bias. The inset in **a** is the original I-V data of this plot.

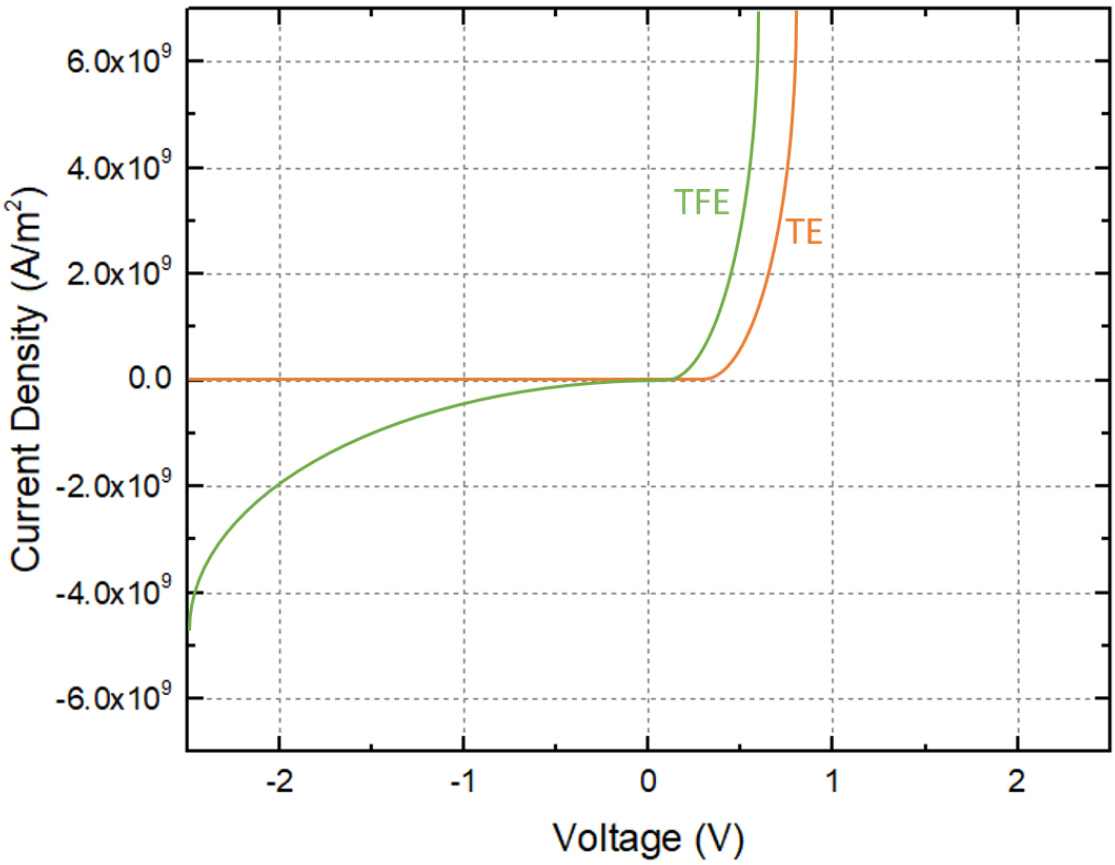

Figure 11 Typical I-V behaviour of thermionic emission (TE) and thermionic field emission (TFE).

Table 1 Fitted parameters of F-N modelling for thickness-dependent and contact geometric electrical test

Test no.	No. of layer(s)	Type of Contact	Estimated Contact Area	Forward Bias		Reverse Bias	
				C1	C2	C1	C2
1	1	Edge	3.27	-16.4	-0.00916	-16.6	-0.00947
2	1	Edge	3.27	-17.0	-0.00855	-17.2	-0.00883
3	1	Edge	1.97	-18.5	-0.0149	-18.8	-0.0157
4	1	Edge	1.20	-18.9	-0.0319	-20.2	-0.0394
5	1	Edge	3.55	-18.2	-0.0177	-18.6	-0.0189
6	6	Face	62.6	-19.3	-0.1712	-19.3	-0.163
7	6	Edge	16.0	-16.1	-0.0809	-16.2	-0.0943
8	3	Edge	8.13	-20.8	-0.230	-19.9	-0.0828
9	1	Edge	2.11	-18.8	-0.147	-19.0	-0.0769
10	1	Edge	1.88	-18.4	-0.0921	-18.3	-0.0596
11	2	Edge	8.54	-19.0	-0.167	-19.0	-0.109
12	2	Edge	6.89	-15.7	-0.0301	-17.1	-0.0342
13	1	Edge	3.98	-15.2	-0.0296	-16.0	-0.0522
14	1	Edge	1.28	-17.3	-0.0356	-17.8	-0.0432
15	1	Edge	3.74	-18.3	-0.169	-18.4	-0.0722

16	1	Edge	3.61	-19.0	-0.230	-19.0	-0.161
17	6	Face	51.9	-19.4	-0.259	-19.2	-0.169
18	6	Face	42.2	-19.3	-0.283	-19.4	-0.271
19	6	Face	44.4	-18.8	-0.233	-18.8	-0.174
20	6	Face	27.6	-19.0	-0.271	-19.0	-0.224
21	6	Face	29.1	-18.7	-0.234	-18.6	-0.164
22	6	Face	24.2	-18.8	-0.246	-18.8	-0.210
23	3	Edge	5.32	-20.5	-0.311	-20.6	-0.359
24	2	Edge	4.34	-20.5	-0.335	-20.6	-0.370
25	2	Edge	3.33	-19.5	-0.361	-19.6	-0.339
26	6	Edge	42.5	-18.9	-0.272	-18.9	-0.236
27	6	Edge	41.0	-19.0	-0.305	-19.0	-0.264
28	6	Edge	40.9	-18.9	-0.293	-19.0	-0.256
29	6	Face	21.4	-18.9	-0.344	-19.0	-0.314
30	6	Face	23.2	-18.5	-0.263	-18.5	-0.251
31	6	Face	44.7	-18.1	-0.223	-18.2	-0.196
32	1	Face	9.40	-18.6	-0.0495	-18.7	-0.0489
33	1	Face	9.31	-18.6	-0.0469	-18.9	-0.0486
34	1	Face	8.29	-18.9	-0.0473	-18.8	-0.0458
35	3	Face	17.8	-18.0	-0.221	-18.1	-0.225
36	3	Face	18.8	-18.2	-0.247	-18.3	-0.233
37	3	Face	18.5	-18.6	-0.323	-18.6	-0.296
38	3	Face	27.8	-18.7	-0.339	-18.8	-0.313
39	6	Face	41.8	-18.6	-0.365	-18.5	-0.340
40	6	Face	41.8	-18.6	-0.369	-18.5	-0.333
41	6	Face	48.8	-18.1	-0.286	-18.0	-0.255

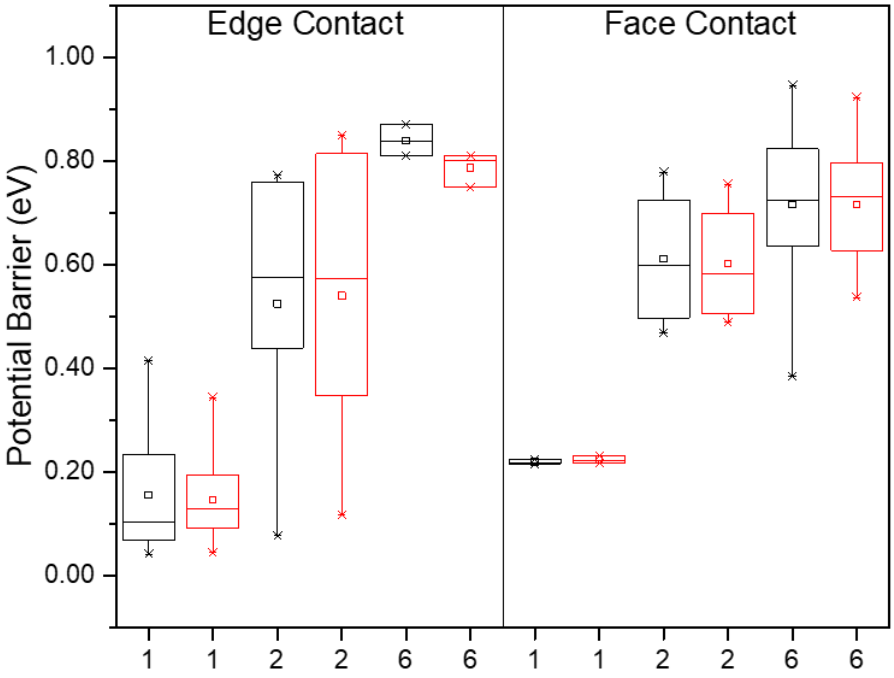

Figure 12 Potential barrier distribution for edge contact and face contact with respect to 1L, 2L, and 6L contact as well as bias direction. Black boxes represent forward bias and red boxes represent reverse bias. The numbers on the x-axis represent the number of layer(s).

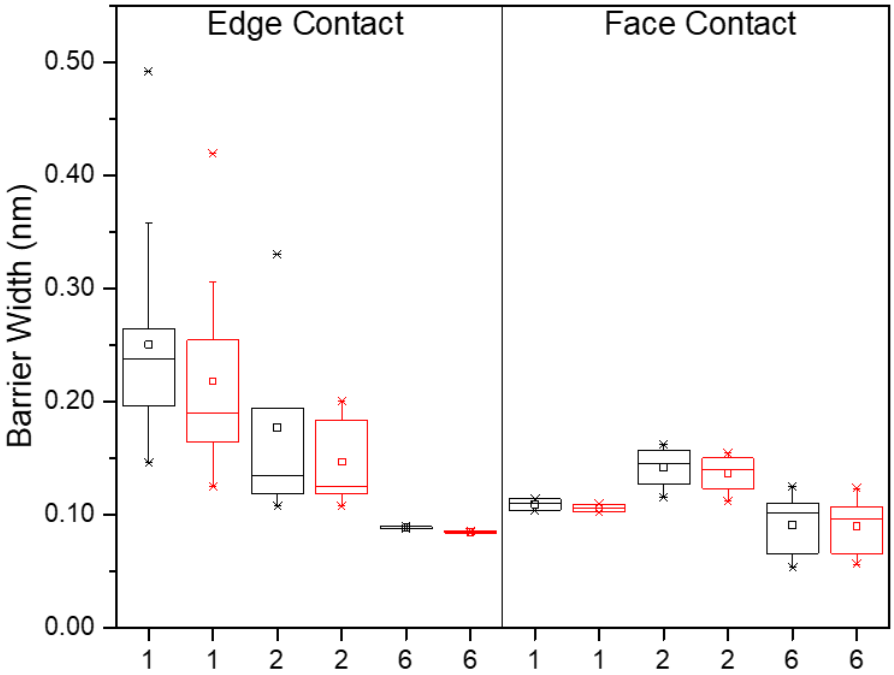

Figure 13 Barrier width distribution for edge contact and face contact with respect to 1L, 2L, and 6L contact as well as bias direction. Black boxes represent forward bias and red boxes represent reverse bias. The numbers on the x-axis represent the number of layer(s).

The thickness-dependent band structures in 2D MoS_2 have been extensively investigated via optical or other methods [91-93]. The potential barriers at the 2D MoS_2-W contacts are caused by the band alignments at the interfaces (**Figure 14**). The reported

electron affinity [92] of 2D MoS_2 is around 4.0~4.3 eV, lower than the work function of W (4.6 eV), yielding potential barriers of 0.3~0.6 eV at the contact in reverse direction (**Figure 14**). On the other hand, the work function of n-type 2D MoS_2 is within 4.1 eV~4.5 eV with thickness dependence [93], therefore the band realignment after contact will create potential differences of 0.1~0.5 eV in forward direction (**Figure 12**). In this highly doped MoS_2 membrane, fermi level is very close to the conduction band and hence the potential barrier of reverse bias which is very close to that of forward bias. In addition, the surface state on 6L MoS_2 edge contact realigns the band structure, and hence the potential barrier of reverse bias is significantly lower than that of forward bias (**Figure 12** and **Figure 14**). This is caused by the larger contact area in 6L MoS_2 edge-on configuration as shown in Fig. 1f-h and the edges are not totally parallel to the W probe, such that the probe only partially contacts with that "6L" MoS_2 and hence creating a huge surface state effect. In other cases, for example, 1L and 2L MoS_2 edge contact as well as face contact. The contact area in those two contacts is much easier to form a perfect contact with the W probe compared with 6L MoS_2 edge contact. In the perspective of face contact, no matter the layer number is increased, the contact area is similar, that implies that the effect of surface state is negligible under face contact with small contact area. Indeed, the probe would provide a small force to the 2D flake when the contact forms (**Figure 15**). Probably, this small force might level the effect of surface state.

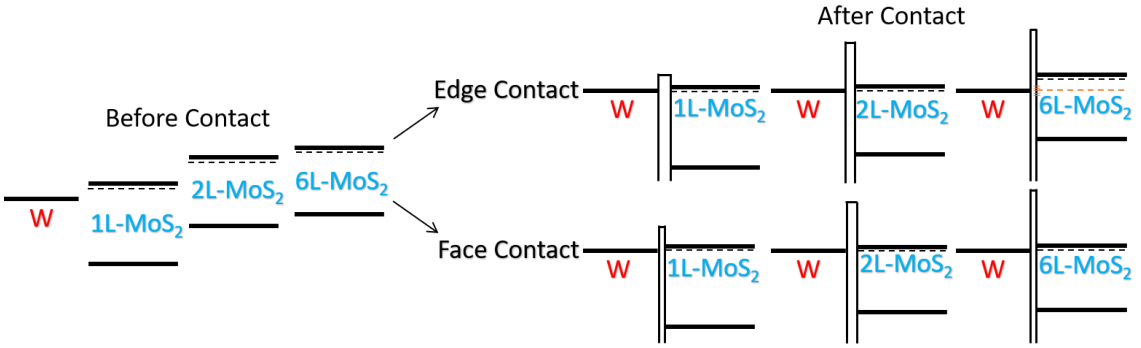

Figure 14 Band diagram for tungsten nanotip and 1L, 2L, and 6L MoS_2 before and after contact based on the results of **Figure 9 & 10**.

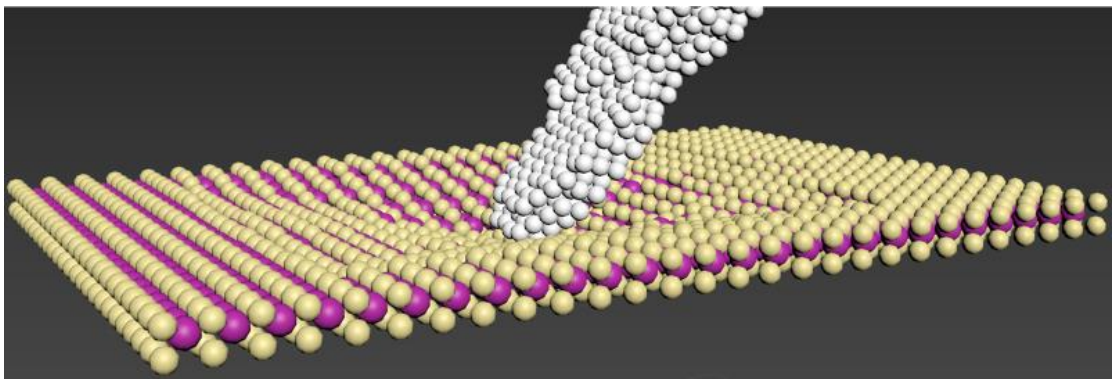

Figure 15 Illustration of small force in face contact.

FE model work well mainly because of the ultra-small widths of barriers for these 2D contacts. The fitted barrier widths for all the face and edge contacts are smaller than the layer thickness (plane distance along *z*-direction) in MoS_2 (0.62 nm), showing the good electron screening and the 2D dimension reduction effects of the 2D MoS_2, and the contact barriers are well-restricted within the first atomic layer of MoS_2. The 2D membranes have strong anisotropic permittivity given by the vdW layered atomic structure, the out-of-plane permittivity for face contact ($\varepsilon_{\perp}$) is 4 times less than in-plane permittivity of edge contact ($\varepsilon_{//}$) (**Figure 13** and **Eq. 12**), hence the barrier widths of face contact are usually smaller than edge contact. The slightly increased barrier width in mono- and bi-layer of MoS_2 edge contacts may be attributed to the reduced carriers/free electron densities by the good contact configurations and less defects remained, as the higher mechanical flexibilities in thinner 2D membranes will assure the better conformations at the interface edges.

A CVD grown MoS_2 monolayer was also tested. A relatively clean 2D MoS_2 was found that and the crystallinity was good by checking the selected area electron diffraction pattern (**Figure 16**). Three contact sites were selected to employ I-V measurements. In **Figure 17-Figure 19**, the contact locations, I-V plots, and F-N fitting of W probe-CVD 1L MoS_2 contact were displayed. The I-V plots were symmetric, and the F-N fits coincided with the data points that field emission was dominant in this M-S nano-contact. On the other hand, the potential barrier distribution and barrier width distribution without considering contact geometry this time can be seen in **Figure 20-Figure 21**. The potential barrier of this test was higher than the former tests, but the barrier width of this test was lower. Similar to the previous results, the reverse bias demonstrated a lower potential barrier than forward bias, but the decrease of potential barrier was larger than the exfoliated 1L MoS_2. The apex of W probe was about 8 nm which was close to the former test and the probe was more uniform in shape than the former one. Although the difference between exfoliated MoS_2 and CVD grown MoS_2 was huge, the sample size was still low. The results can only provide a preliminary insight into the barrier formation. In a summary of the barrier formation of the F-N tunnelling, the rectangular shape barrier had a certain degree affected by the probe size and shape as well as the synthesis method of the MoS_2.

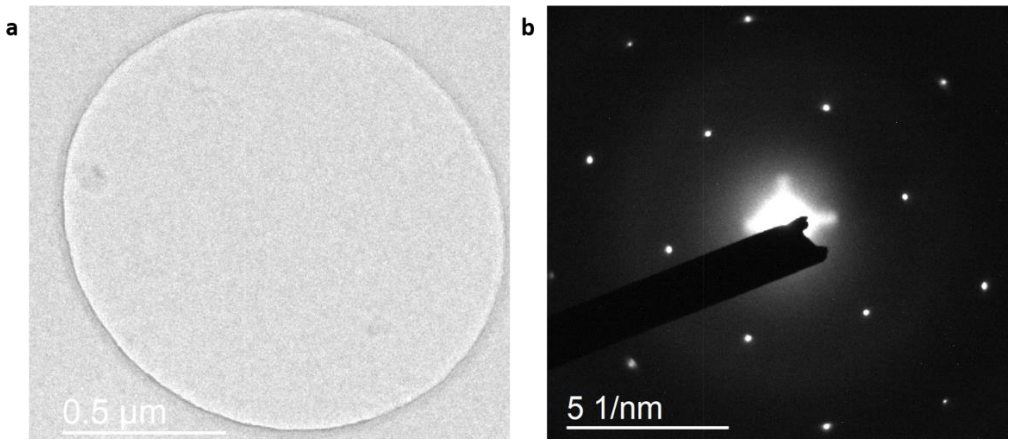

Figure 16 a TEM image and **b** selected area electron diffraction pattern of CVD grown 1L MoS_2.

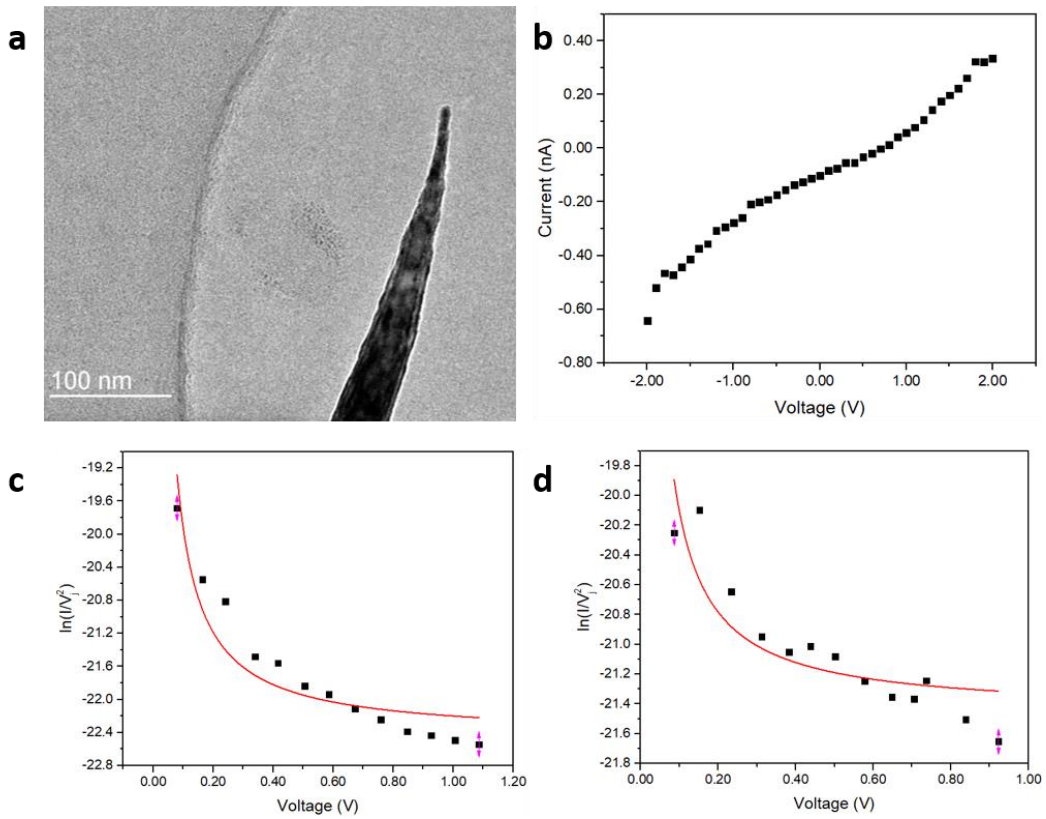

Figure 17 a TEM image of the M-S nano-contact. **b** I-V plot of the corresponding contact. F-N fits of **c** forward bias, and **d** reverse bias.

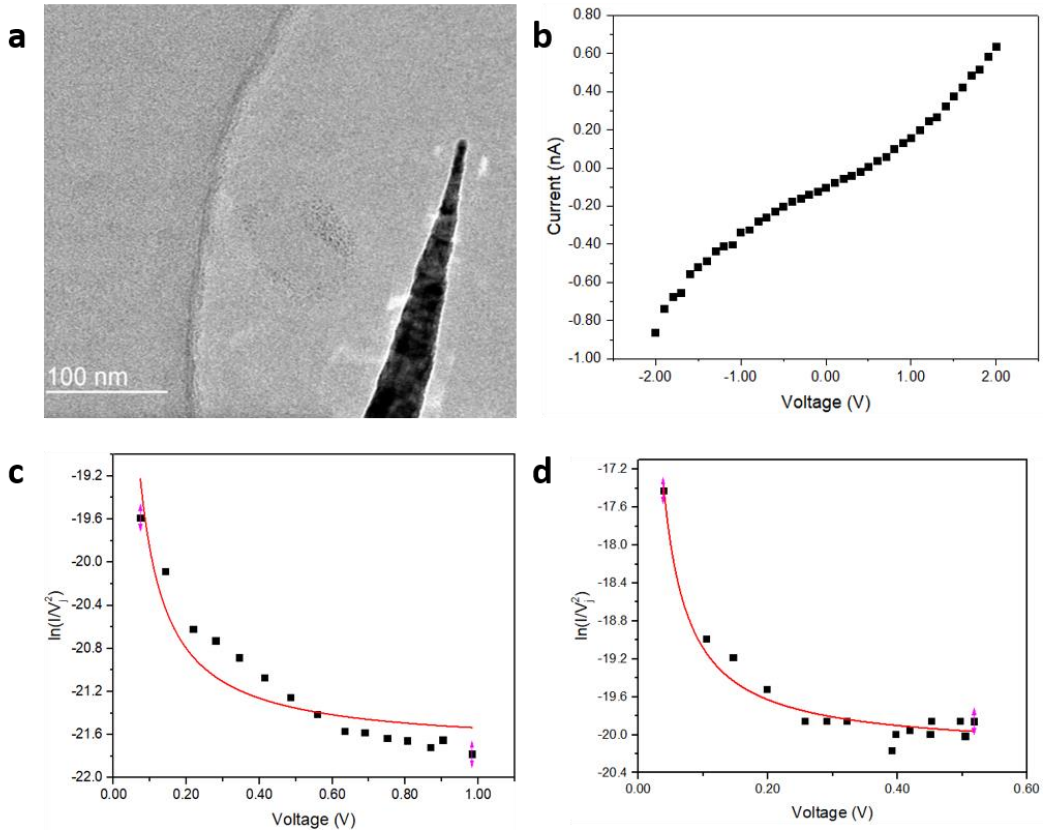

Figure 18 a TEM image of the M-S nano-contact. **b** I-V plot of the corresponding contact. F-N fits of **c** forward bias, and **d** reverse bias.

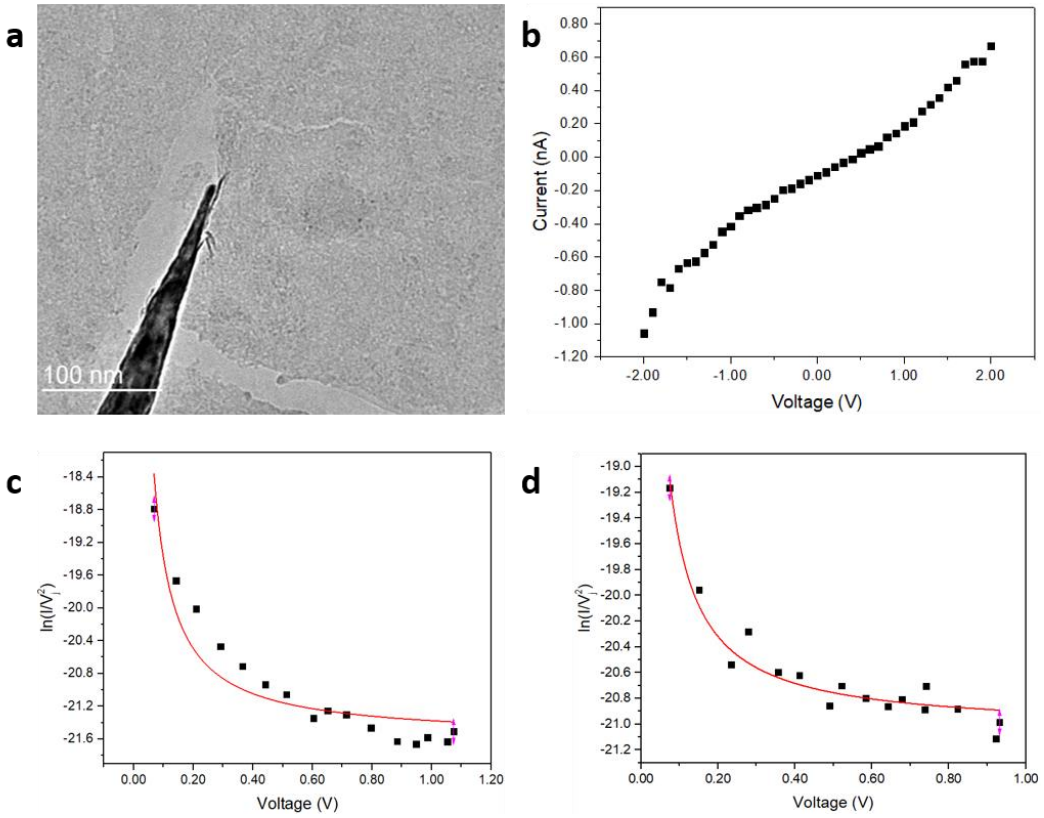

Figure 19 a TEM image of the M-S nano-contact. **b** I-V plot of the corresponding contact. F-N fits of **c** forward bias, and **d** reverse bias.

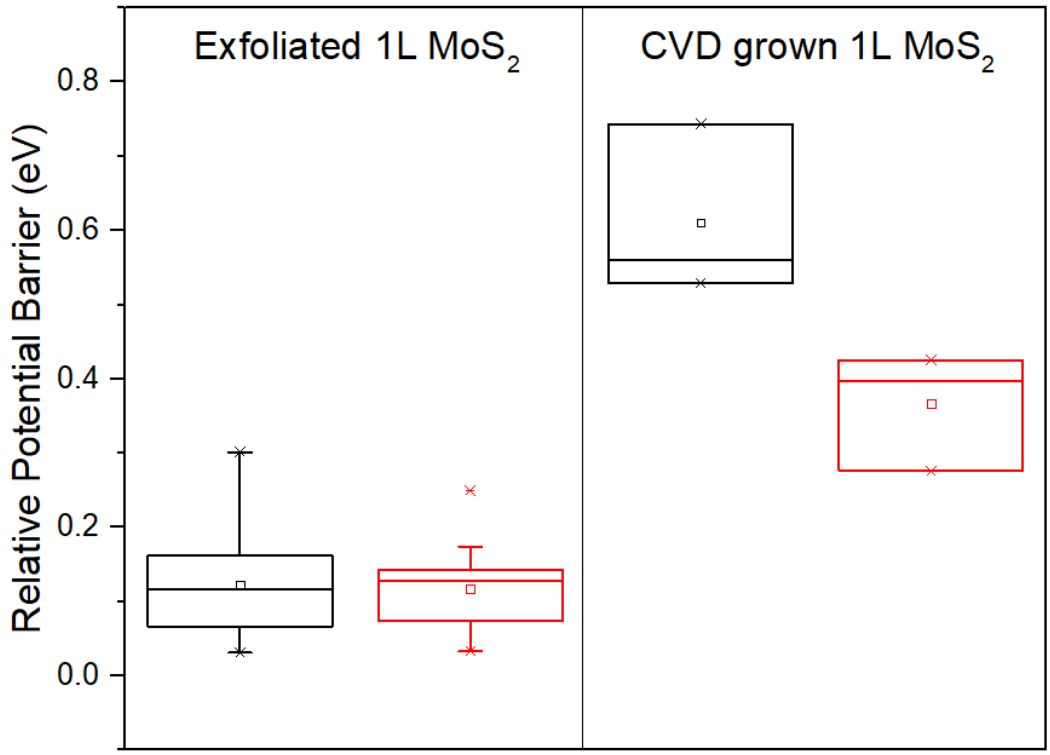

Figure 20 Potential barrier distribution for the M-S contact of exfoliated 1L MoS_2 and CVD grown 1L MoS_2 with bias direction. Black boxes represent forward bias and red boxes represent reverse bias.

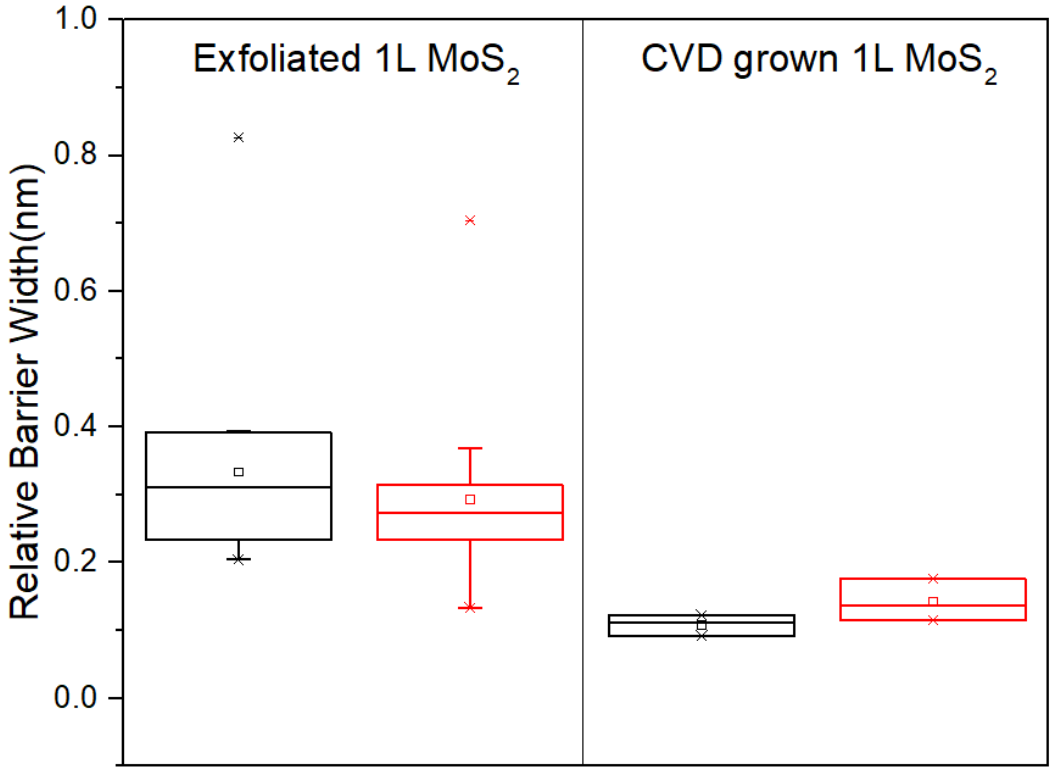

Figure 21 Barrier width distribution for the M-S contact of exfoliated 1L MoS_2 and CVD grown 1L MoS_2 with bias direction. Black boxes represent forward bias and red boxes represent reverse bias.

3.3. Stress-Dependent Electrical Properties

There were two stress-dependent electrical tests would be introduced. The first one was the exfoliated 6L MoS_2 and the second one was the CVD grown 1L MoS_2. The first one only covered a half grid; the W tip was under the 6L membrane and made a contact (**Figure 22a**). The I-V measurements were tested when the tip was moved upward (in z-direction) with a certain distance that provide the stress on the membrane (**Figure 22b**). The conductivity slightly increased with stress. Due to the symmetricity, the F-N fitting had been applied to all I-V data. Hence, the effect of the stress in potential barrier and barrier width was found (**Figure 22c-d**). The potential barrier was decreased with the increasing stress while the barrier width was increased with that. On the other hand, a full grid 1L MoS_2 was contacted by a W tip (**Figure 23a**). The I-V measurements were also tested when the tip applied different stress onto the membrane and the conductivity was

decreased when the stress increased (**Figure 23b**). Finally, the potential barrier was independent of stress which held around 0.69 eV but the barrier width was dropped with the increasing stress (**Figure 23c-d**). The upward test would change the boundary condition since the membrane was put away from the supporting grid. This may affect the stress test. In the second one, the tip pressed on the near the grid, that provided an imbalance force. That may also affect the stress test. The tip should press around the middle of the membrane, that can simplify the studies, even in the theoretic calculation.

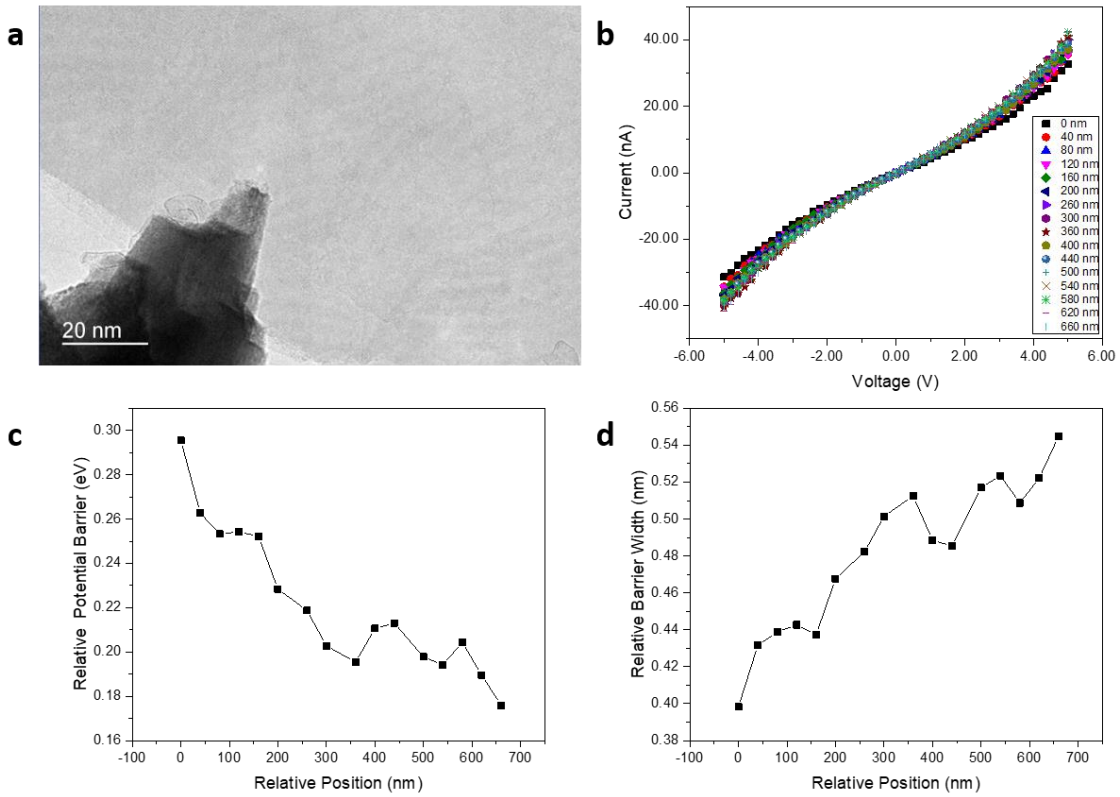

Figure 22 a TEM image of W-6L MoS_2 contact. **b** I-V plot with different z-direction from the original contact point. The stress-dependent **c** potential barrier and **d** barrier width.

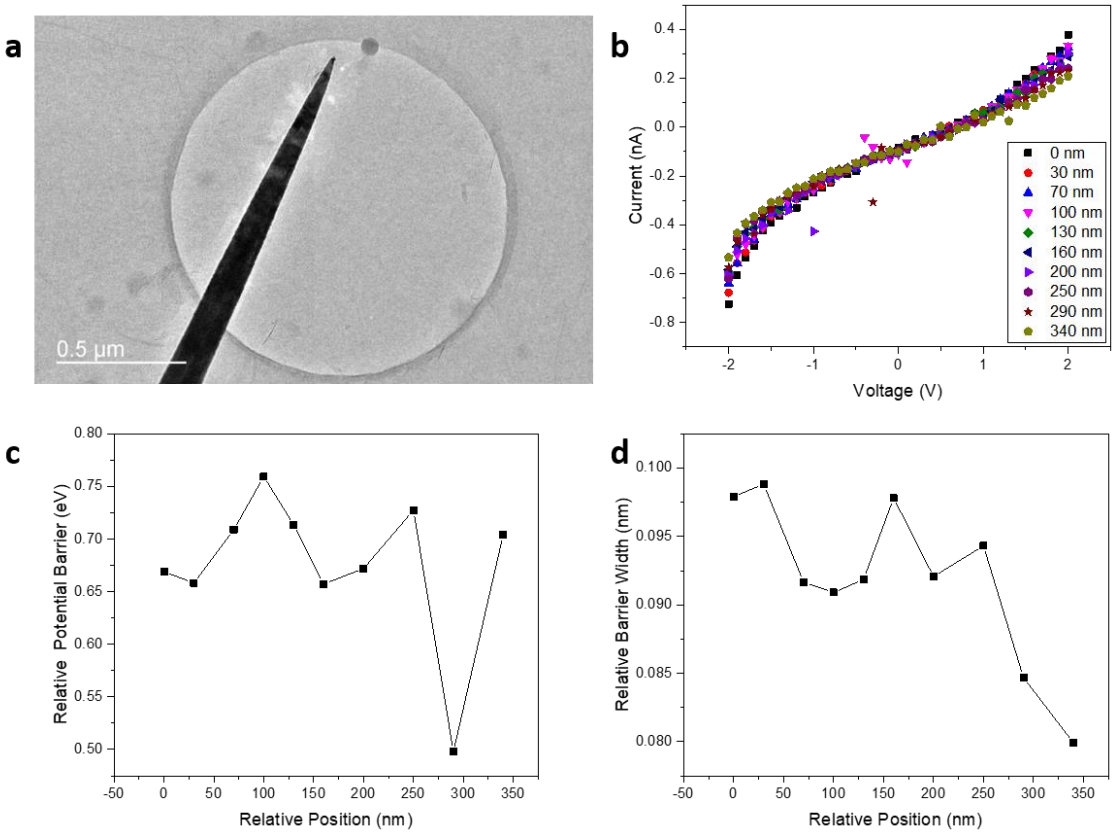

Figure 23 a TEM image of W-1L MoS_2 contact. **b** I-V plot with different z-direction from the original contact point. The stress-dependent **c** potential barrier and **d** barrier width.

3.4. Screw Dislocation Induced Conductivity

The effect of crystal defects is distinct in 2D contacts. Except for the results above, it can be further demonstrated by the *in situ* formed/annihilated screw dislocation. In a 6L face contact (edge-on view) measurement, a screw dislocation was observed to emerge from perfect layers (**Figure 24**, 17 s, **supplementary video 2**), induced by the local shear strain (scheme shown in **Figure 25**, also see **supplementary video 3**). The excess layer edge on the top after half unit cell slip (also burger's vector $=\frac{1}{2}\hat{z}$) through the layers during screw dislocation formation could be visualized (**Figure 24b-c**). The screw dislocation existed for 6 s and then disappeared (**Figure 26**, 3 s, **supplementary video 4**). The contact zone was totally recovered after the annihilation of the screw dislocation. The **supplementary video 2** and **4** presents this entire process. The atomic model and TEM

image simulation by multislice method (**Chapter 2.5**). **Figure 27** was built and tested for the screw dislocation core, the result coincides with our *in situ* TEM observations. Besides, this screw dislocation is reversible, which self-healing of screw dislocation in few-layer MoS_2 has been observed, but the mechanism has to be further studied.

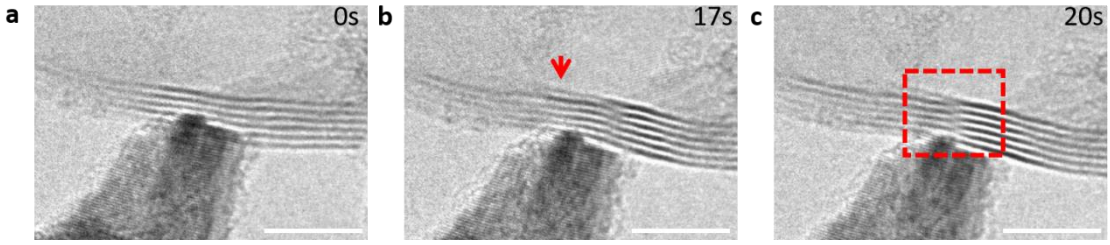

Figure 24 TEM images of the form of the screw dislocation during measurement at **a** 0 s, **b** 17 s, **c** 20 s. Scale bar: 5 nm.

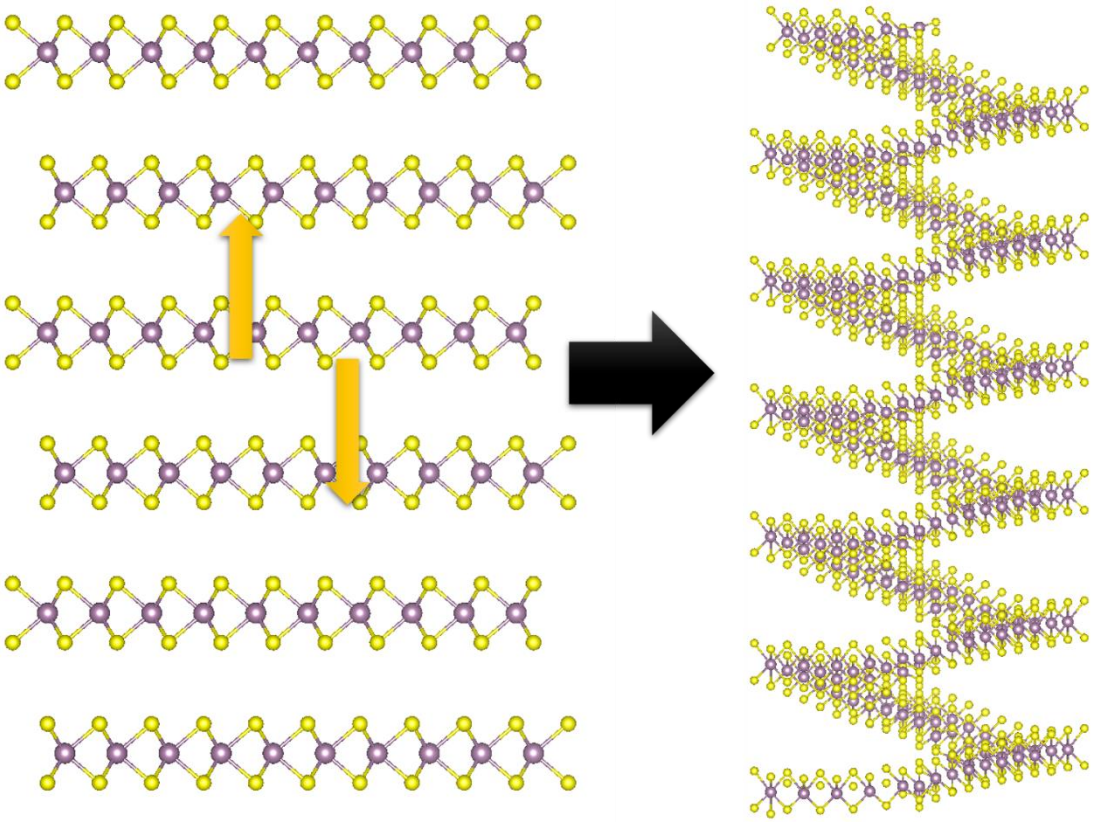

Figure 25 Scheme of local shear strain including action and reaction force.

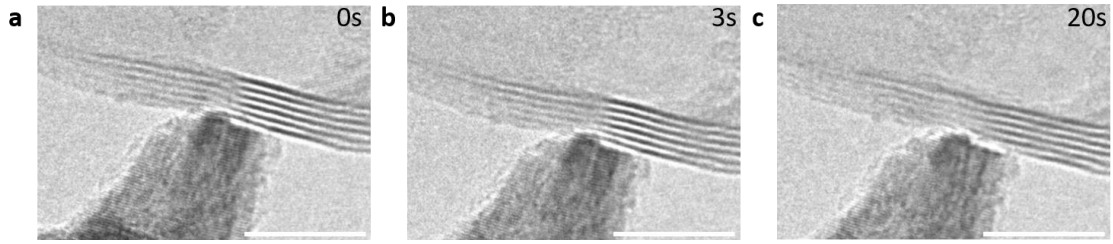

Figure 26 TEM images of annihilation of the screw dislocation during measurement at **a** 0 s, **b** 3 s, **c** 20 s. Scale bar: 5 nm.

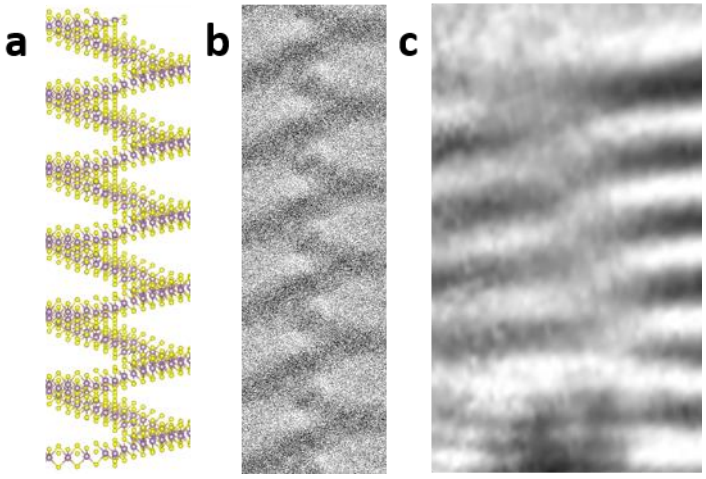

Figure 27 a Atomic model (VESTA), **b** simulated HREM image (multislice in jems), and **c** experimental image enlarged from the red dash box in **Figure 13c** along zone axis [010].

Two I-V measurements (±2.00 V scan) were simultaneously carried out through the above process. It can be seen the conductance was abruptly enhanced when the screw dislocation was formed. In specific, the conductance was risen from 2.00 to 3.88 nS (**Figure 28a**). Vice versa, when the screw dislocation annihilated, the conductance returned to the origin, decreased from 4.81 to 2.39 nS (**Figure 28b**). Thus, the screw dislocation increased the system conductance by nearly 100%, which is in strong agreement to our CAFM measurements on single screw dislocations [95] (**Figure 29**). Because of the screw dislocation, all the 6 atomic layers were connected and contributed to the transport, rather than relying on the vdW interactions and electron tunnelling in perfect multilayer MoS_2. The conductance enhancement by screw dislocation was widely found in many other materials [96-98], however, much higher conductance was gained by single dislocation in 2D contacts due to the change from vertical transport into in-plane transport.

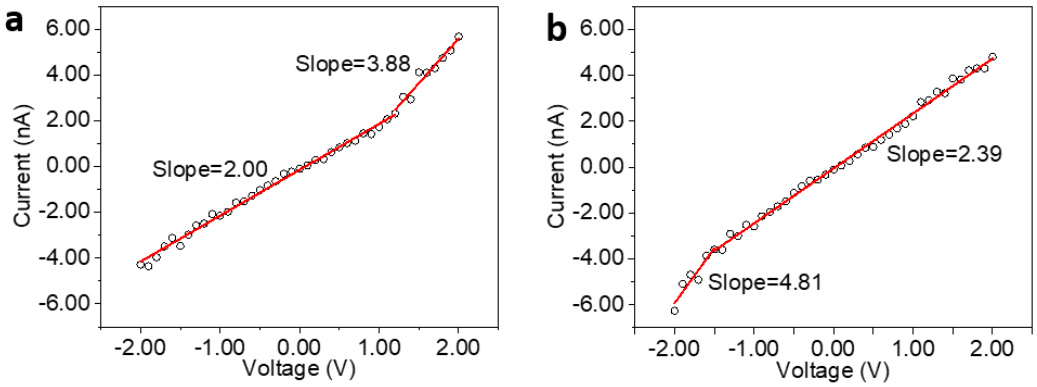

Figure 28 I-V plots for the measurements of **a Figure 24** and **b Figure 26**.

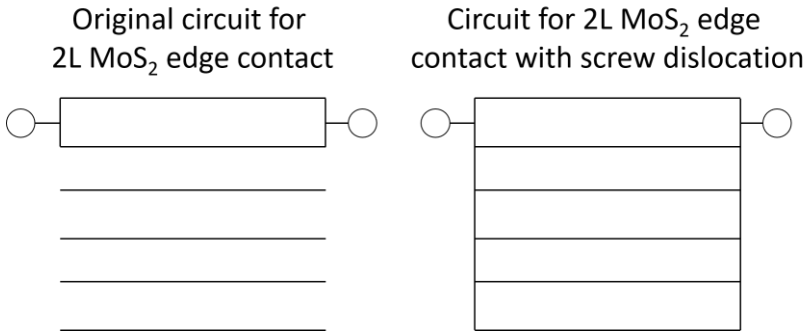

Figure 29 Circuit of the 2L MoS_2 edge contact before and after screw dislocation emerges.

3.5. Different Metal Probe

In order to study M-S contact, different work function would be considered. As mentioned in **Chapter 2.6**, the probe was attempted to be modified by welding a silver nanowire in a parallel direction. The welding experiment was attempted at least 30 times, but only 1 completed welding a silver nanowire. The process of the success 1 will be shown below. A silver nanowire was first approached by a W tip and the electrical bias was applied gradually as seen in **Figure 30**. A breakdown can be clearly observed in the I-V plot that a sharp drop of the current at 6.00 V (**Figure 30b-c**). A part of the nanowire was welded onto the tip with an undesired direction and ball-shaped vertex. Then, the tip approached another silver nanowire and tried to weld the silver nanowire onto the tip (**Figure 31**). Similar to the previous one, a breakdown voltage occurred at 5.60 V and a part of the nanowire was twisted and attached to the tip. Since it just attached to the tip

and hence it lost when the tip approached another nanowire. In **Figure 32**, the third silver nanowire was approached and welded by electrical bias. This time succeeded to weld a silver nanowire onto the tip with the desired direction. This welding was benefited by the previously welded nanowire on the tip. In **Figure 32b**, that welded nanowire became a joint to fix the direction of the twisting nanowire and the twisting force would bend the nanowire as seen in **Figure 30** and **Figure 31**. In **Figure 32c**, the two twisted points can be observed which was induced by bias. The first one was close to the W tip and the other one was the end of the nanowire which was broken in the nearly middle of the whole silver nanowire. The breakdown was about 2.20 V this time (**Figure 32d**). Although electro-breakdown should be the main mechanism of the silver nanowire [24], the Joule heating was also significant. The strong welding in **Figure 30b** implied that the nanowire must be melted and then welded onto the tip. Otherwise, the weak attraction liked **Figure 31c** would easily be removed. In **Figure 32**, electrical driven twisting made the nanowire self-twisting and the thermal energy high enough to melt the attached nanowire as solder to solder the target nanowire. Therefore, it is difficult to confirm whether the target nanowire was broken-down thermally or electrically. However, the other end of the target nanowire was broken without synthesizing a ball shape which meant the other end of target nanowire was probably solely electrical breakdown. Eventually, the Ag nanowire probe attempted to contact a multilayer MoS_2 membrane and the I-V plot behaved as typically TFE (**Figure 33**). The work function of Ag nanowire is around 4.2 eV [99] which is close to the work function of W around 4.5 eV. There was no effect on to the original band structure even the work function had a slight change. However, the silver nanowire in ultrahigh vacuum silver can contact intimately [22], that made the I-V characteristic change. There was only one set of data since the nanowire was shortened and the ball between the

nanowire and the tip hindered the contact. Hence, the other probe measurements have to be attempted in the future again.

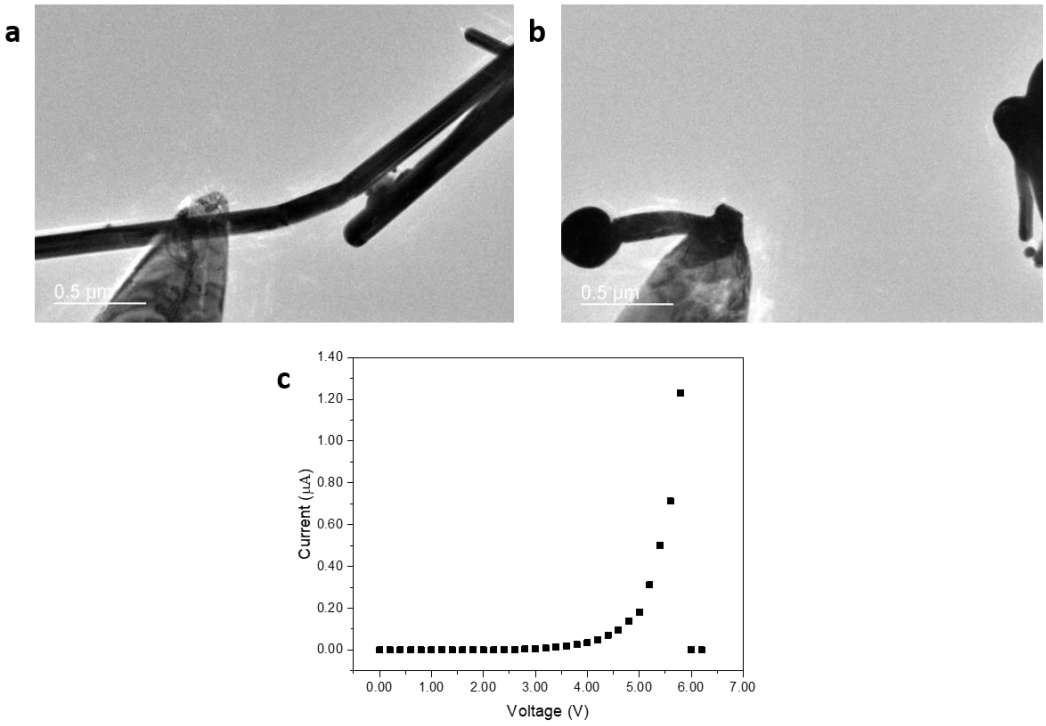

Figure 30 TEM images **a** before and **b** after applying bias. **c** I-V plot for the welding.

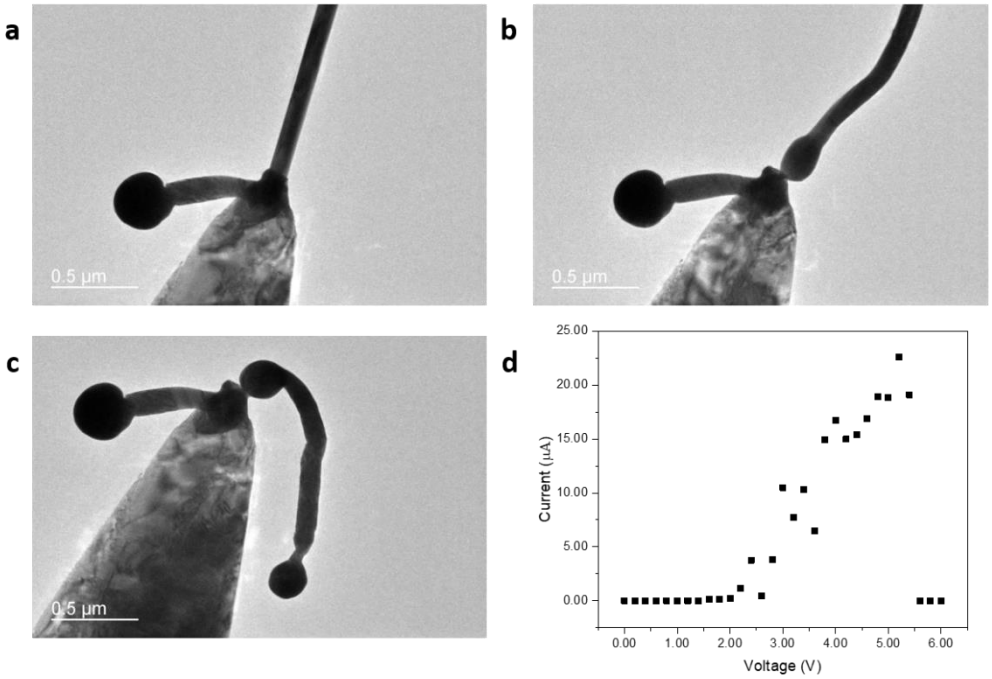

Figure 31 TEM images **a** before and **b** after applying bias. **c** TEM image after a slight pulling. **d** I-V plot for the welding.

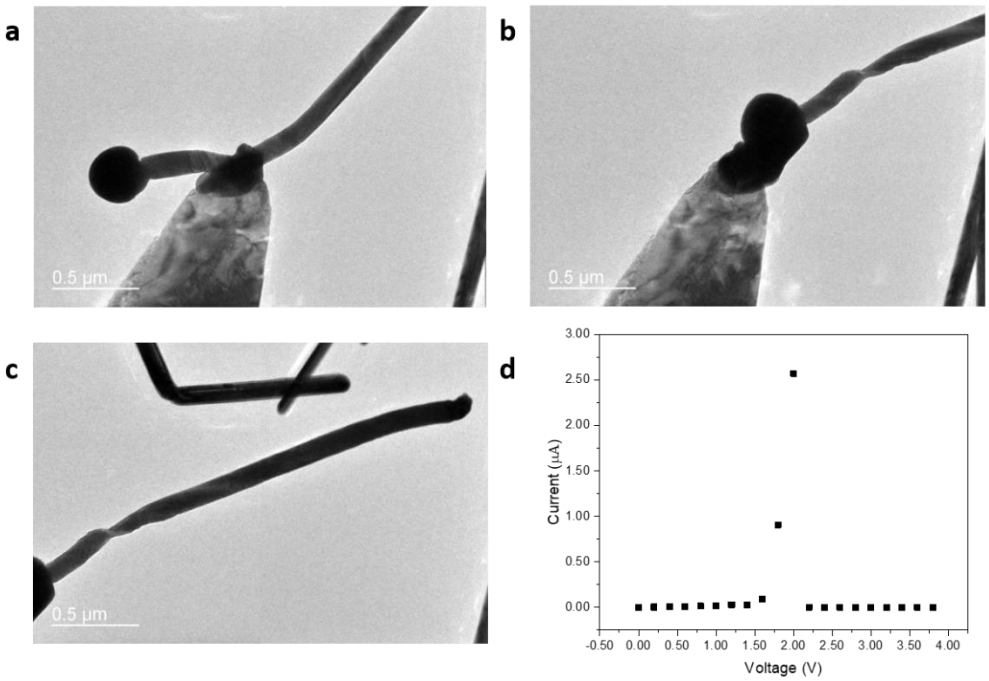

Figure 32 TEM images **a** before and **b** after applying bias. **c** TEM image after a slight pulling. **d** I-V plot for the welding.

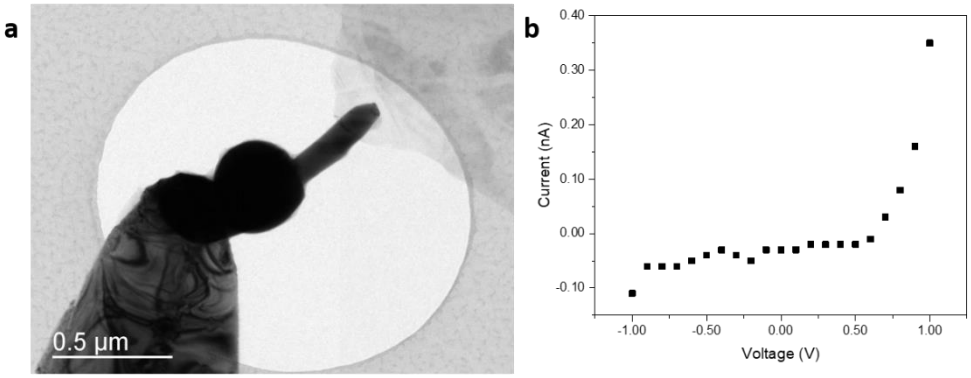

Figure 33 a TEM image of Ag-MoS_2 contact and **b** I-V plot of the Ag-MoS_2 contact.

3.6. *In Situ* Observations of Welding

Other than screw dislocation, welding was observed under a high bias voltage electrical measurement (**Figure 34**). When the I-V measurement started, a part of the W probe was welded immediately. The flake on the tip should be WO_3 since the W probe had been etched before the experiment and the melting point of WO_3 is much lower than that of W. It was unexpected that WO_3 flake was melted firstly rather than few-layered MoS_2. The corresponding I-V plot can be seen in **Figure 35** and the I-V characteristic

behaved like TFE compared with **Figure 11**. The Joule heating generated by ±10.00 V I-V measurement was at least 1298 K so that the WO_3 melted in ultra-high vacuum. This electrical contact was different from the previous results that the WO_3 and few-layered MoS_2 were contacted intimately, similar to **Chapter 3.5**. This was an alternative evidence to prove the previous electrical contacts followed FE.

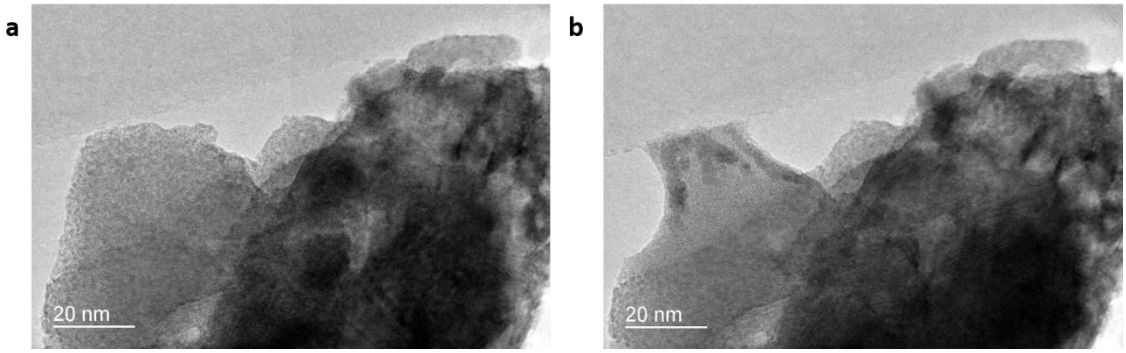

Figure 34 TEM images captured from the video **a** before I-V measurement and **b** at the beginning of the measurement.

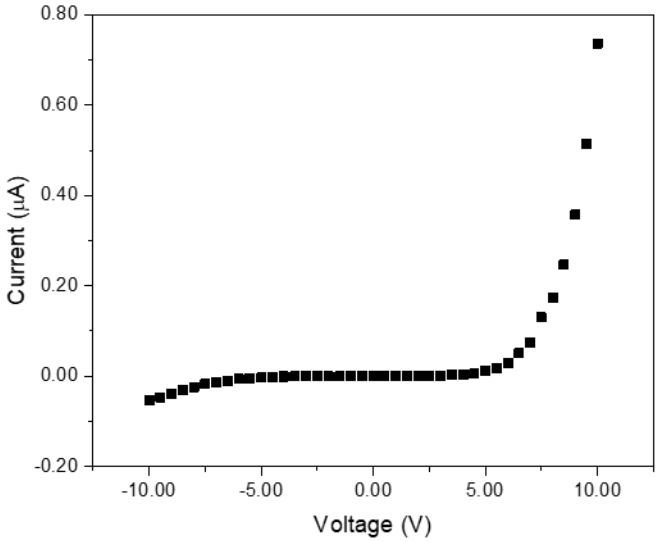

Figure 35 I-V plot of the I-V measurement of **Figure 34**.

3.7. Mechanical Loading Test of Ultrathin Titanium Alloy Film

A FIB cut titanium alloy (Ti/WC) ultrathin film was made by **Dr. YU**'s group and the loading test was employed to the film (**Figure 36**). This specimen had an intrinsic hole which was predicted that the crack would expend during the loading test because of the concentrated strain. However, a loading induced crack was firstly observed along a

grain boundary rather than from the hole in **Figure 36b**. That implied the grain boundary was the weakest part of Ti/WC that was unexpected. The STEM-HAADF image and STEM-EDX mapping were showed a splintered grain boundary of Ti/WC (**Figure 37**). The grain boundary was very weak due to the loose structure. In **Figure 37b-f**, the bonding of grain boundary can be clearly analysed that Co was doped into undesired grain boundary and hence the zig-zag grain boundary was formed. Consequently, the strain applied by the loading test would concentrate on the grain boundary rather than the intrinsic hole. Thus, this is why the crack was along the grain boundary.

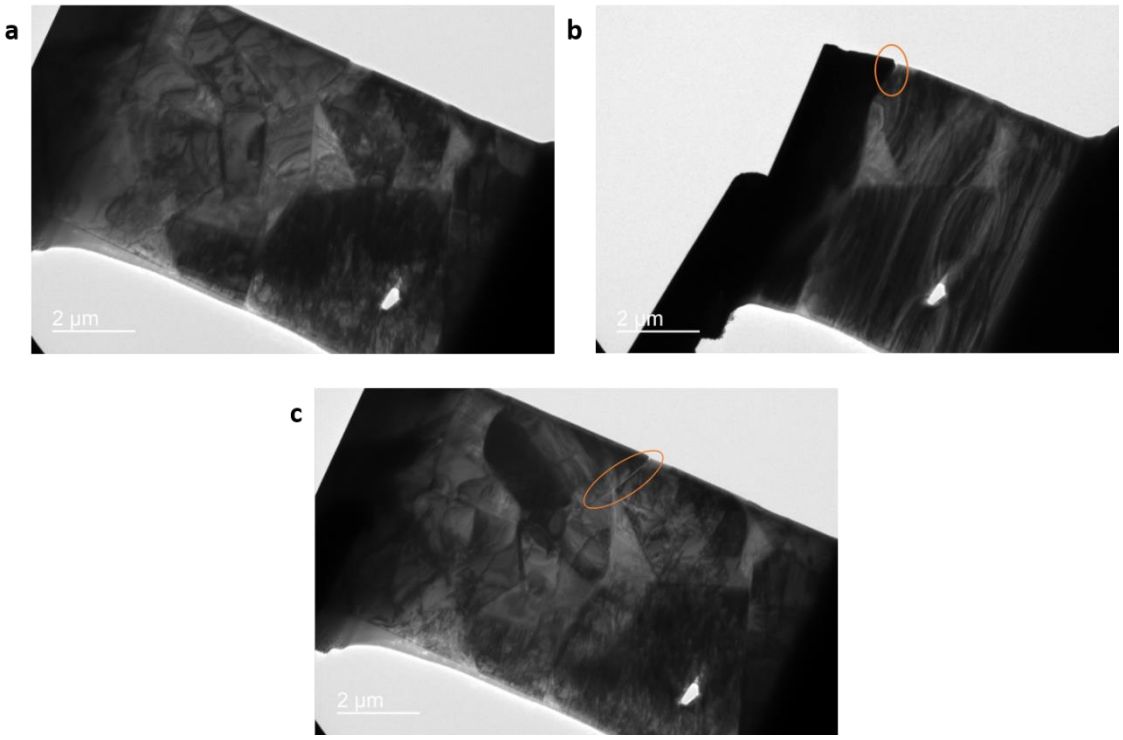

Figure 36 TEM images of Ti alloy captured **a** before loading test, **b** during loading test, and **c** after loading test. The orange circle indicates the crack.

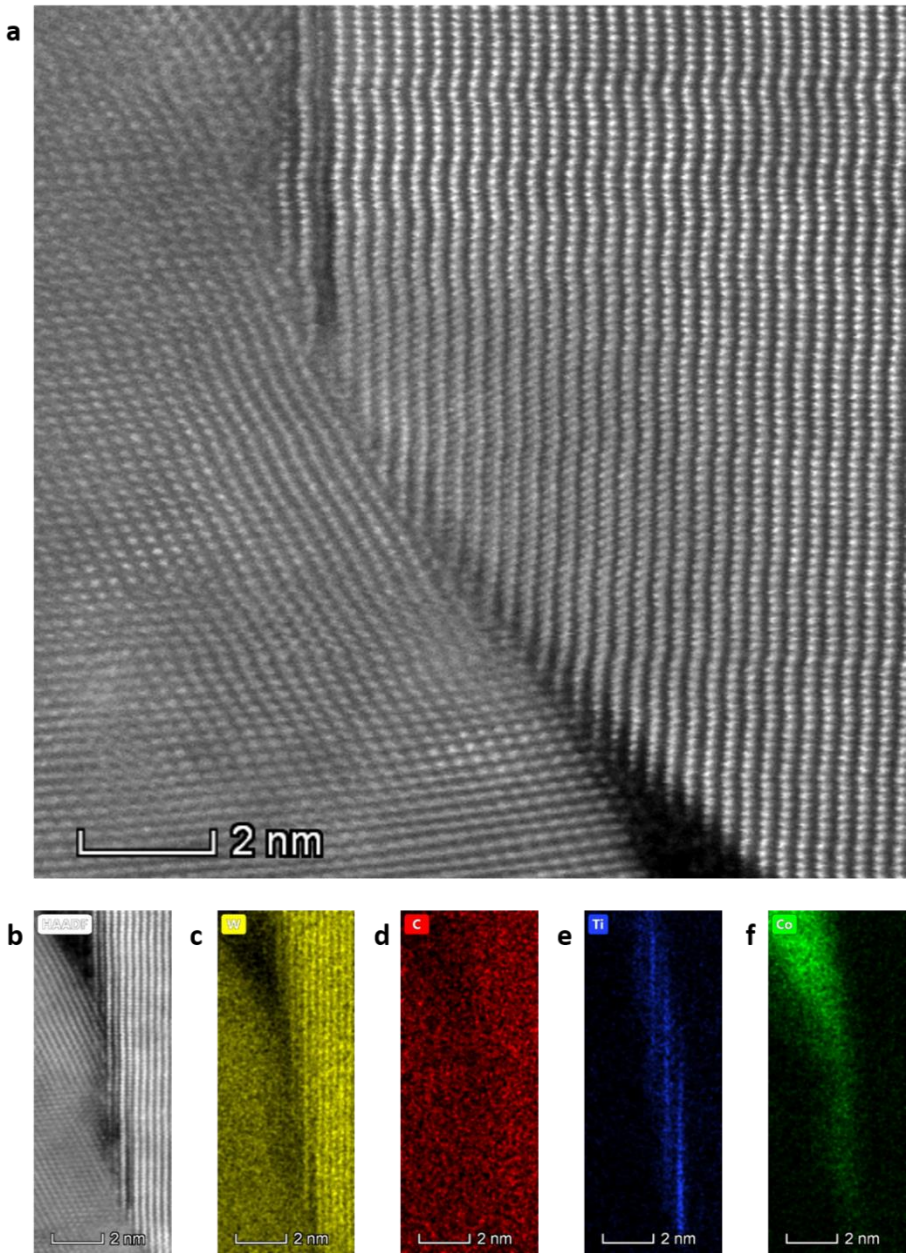

Figure 37 a STEM-HAADF image of Ti alloy. STEM-EDX mapping of **b** interested area and the elements, which are **c** W, **d** C, **e** Ti, **F** Co.

The SDK Ti alloy (Ti/WC/Co) ultrathin films were also tested and their STEM-ABF images were pictured which clearly showed the grains (**Figure 38-Figure 40**). Similar to the previous loading test, three SDK Ti alloy ultrathin films were bent until a crack was noticed. Interestingly, two films were found that the crack was created near centre. The remaining one was cracked from the margin. All ultrathin films demonstrated high flexibility and the cracks were created when the bending was about 90^{o}. The cracks are

waiting for further analysis by Cs-corrected TEM to verify the crystal planes and their structures, so the further results will be reported in the future.

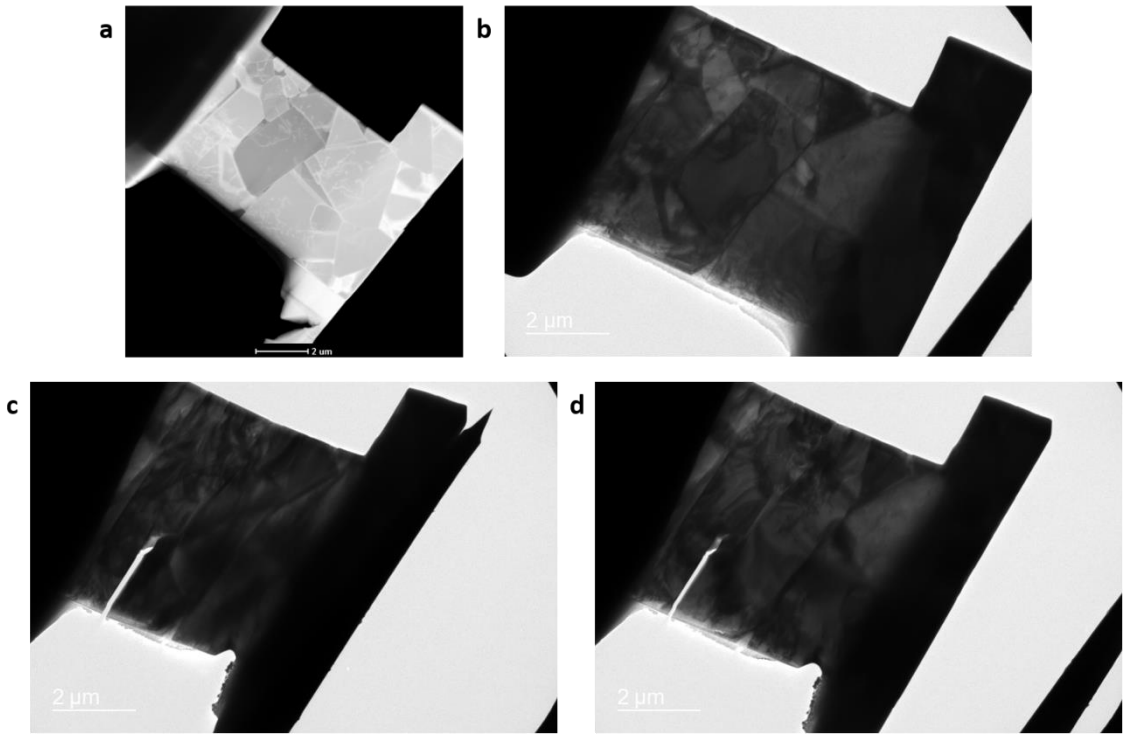

Figure 38 a STEM-ABF image of Ti alloy for crystal plane analysis. TEM images of Ti alloy captured **b** before loading test, **c** during loading test, and **d** after loading test.

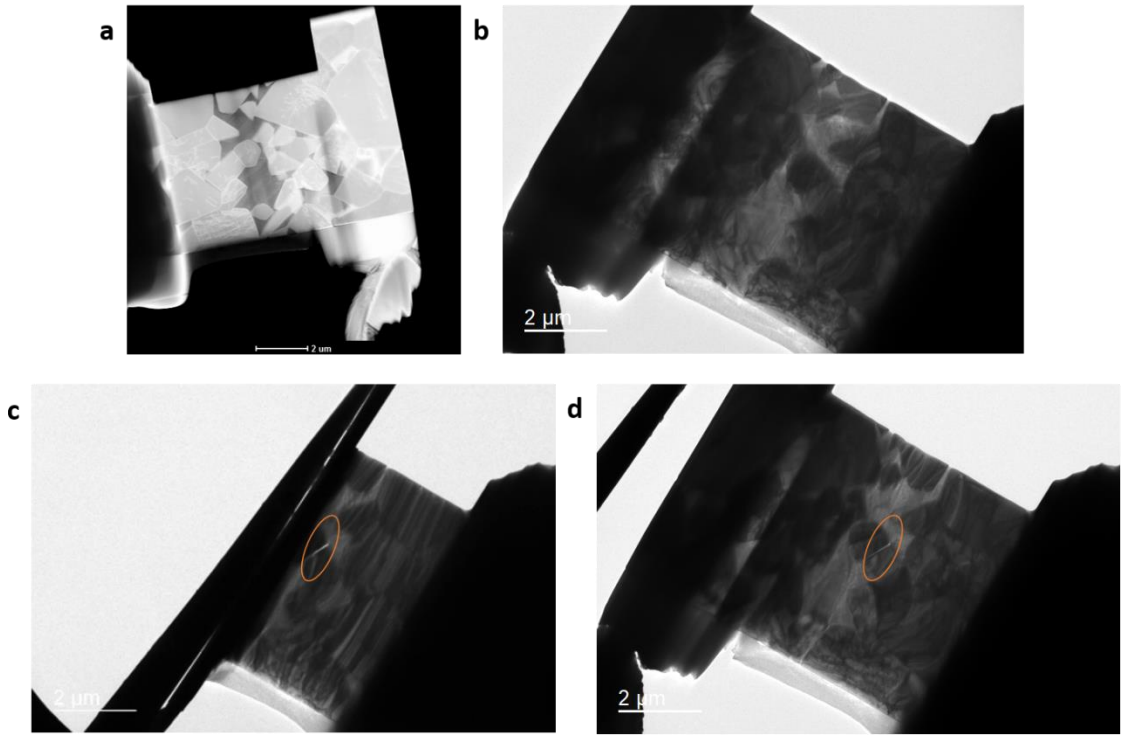

Figure 39 a STEM-ABF image of Ti alloy for crystal plane analysis. TEM images of Ti alloy captured **b** before loading test, **c** during loading test, and **d** after loading test. The orange circle indicates the crack.

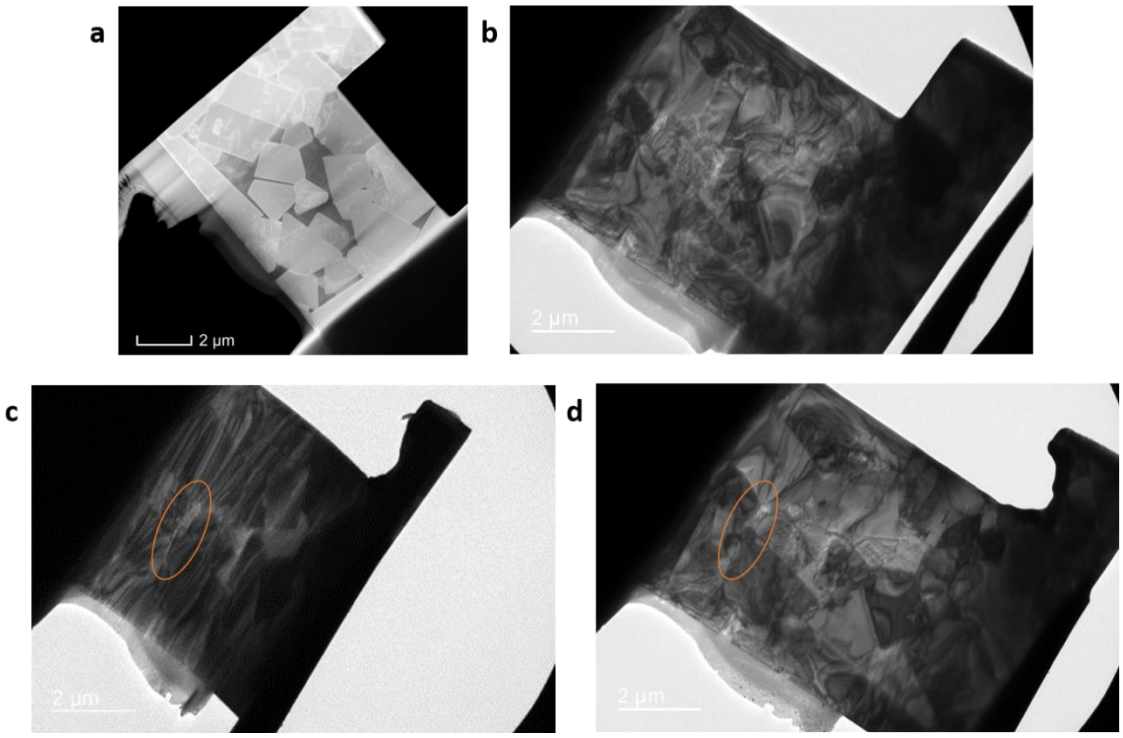

Figure 40 a STEM-ABF image of Ti alloy for crystal plane analysis. TEM images of Ti alloy captured **b** before loading test, **c** during loading test, and **d** after loading test. The orange circle indicates the crack.

Chapter 4. Discussions

All TEM characterizations with *in situ* manipulations have been presented. Real-time measurements have implicated many fundamental properties of 2D materials. The dynamic changes induced by direct stimulations have been recorded and analysed. *In situ* manipulations with TEM characterizations provide a platform for observing the structure-function relation in low-dimensional materials, especially for the promising materials such as graphene and 2D TMDCs. This chapter is going to provide the interpretation of the results, discuss the implications, acknowledge the limitations, and plan the future experiments in both mechanical and electrical properties. In first, electron beam damage in electron microscope get more attention recently, and the irradiation damage will be firstly discussed which affects all measurement under TEM. Afterwards, electrical properties will be discussed secondly, followed by mechanical properties.

4.1. Irradiation Damage

JEOL 2100F with 200 kV accelerating voltage was employed in all experiments above. The irradiation damage is mainly knock-on damage and heating [35-37]. However, the electron dose was controlled under 1 C/m^2 in all experiments. No apparent damage was discovered on the membranes by electron beam during the experiments. In terms of electrical measurements, the I-V plots for the same spot were highly reproducible which also implies the minimized beam damage. The heating up by the electron beam can be estimated by the thermal conductivity of the membranes with the dose [100, 101] and the temperature rise is within 20 K. In short, the defects involved in the membranes were mainly intrinsic or induced by *in situ* manipulations.

4.2. *In Situ* Electrical Measurements

2D materials have been widely reported to be next-generation devices promisingly [16-18, 42, 48]. Owing to uncompleted fundamental studies of nano-contact, here, parts of mechanical and electrical properties have been unravelled for understanding the mechanisms which benefits the future design of the next-generation devices. The thickness-dependent electrical conductivity in the nano-contact has been confirmed that the conductivity is decreased with the increase of thickness in both edge contact and face contact. Different from the transistor-based thickness-dependent measurement, all electrical properties in this thesis has been measured from the same MoS_2 membrane. Because of the symmetricity of the I-V plot and the F-N fitting, field emission should be dominant in the transport. Thus, the trend of thickness-dependent conductivity is possibly caused by the increasing potential barrier and decreasing barrier width of vdW gap between the M-S nano-contact. Interestingly, the formation and annihilation of a screw dislocation has been observed during the I-V measurement due to the mechanical force. The magnetic field inside TEM is perpendicular to the current flow through the M-S contact. Real-time response of the I-V plot suggests that the conductivity was around double when the screw dislocation was formed. Another strong evidence of the screw dislocation induced conductivity change is the annihilation of the screw dislocation in the very next measurement that real-time response of the I-V plot indicates the conductivity is half. The screw dislocation has been confirmed by simulated images, acts like a switch that turns the circuit all in parallel. Joule heating may be one of the concerns to affect the conductivity test, but the temperature rise by Joule heating is estimated below 1 K, which is negligible [101]. This electrical study demonstrates some fundamental insight into the 2D materials.

Unfortunately, the study of electrical properties of nanosheet is incomplete. The I-V measurement in the nano-contact can be only conducted by two-terminal. If the four-terminal measurement can be conducted, more electrical properties can be determined such as hall mobility, sheet resistance and actual conductivity. Although the data can be classified into different layers, hopefully, there will be a better stair-like structure to be studied. Moreover, the sample size is insufficient, only 41 tests are recorded. However, the measurement is difficult to be repeated. It requires an excellent tip with a well orientated stair-like few-layer membrane. However, it is possible to repeat, just need more attempts. There are still many interesting topics will be investigated such as stress-dependent electrical conductivity. The other combination of metal-semiconductor nano-contact can be also attempted.

The CVD grown single-layered MoS_2 was also measured and fitted by F-N modelling. The I-V plots show the good symmetricity of forward and reverse bias, similar to the mechanically exfoliated MoS_2 membrane. However, the fitted results show a huge different in potential barrier that may be caused by the different W tip and the different contaminations on the membranes. In the future, a W tip will be kept even after use. Although there must be some contaminations on the tip, there should be a way to clean the tip. The aim of keeping a tip is to reduce random variables, such as shape and size.

4.3. *In Situ* Welding

Both thermal and electrical breakdown would occur during welding. Thermal breakdown is preferred for welding that forms a better soldering. Electrical breakdown not only breaks the nanowire but also twist the nanowire a lot. However, the control of breakdown is difficult. It will be tried in the future. On the other hand, a special welding

of M-S contact has been observed. The metal part firstly melts rather than the semiconductor. That flake on the tip must be oxide which has a much lower melting point. However, that melting may prove the I-V behaves TFE in hundreds nm-scale when the contact is intimately. This hypothesis needs further investigation to prove. It is suggested to find the condition of the intimate contact in the future.

4.4. *In Situ* Loading Test

The loading test of metallic thin films has been demonstrated. The films would crack along different crystal plane to release strain. If the weakest plane is found, the strongest plane can be found eventually. Hence, the strongest metallic thin film can be fabricated. However, the analysis is still ongoing. Thus, the analysis will be finished in the future. It is recommended to use around 500 nm diameter tip to implement the mechanical loading test, because of the strength of the tip. Based on the experience, the optimal loading can be applied by this condition. If the tip is too small, the strength is insufficient for bending the potential stored by the bending membrane. On the contrary, the tip is too large, the tip would hinder the observation of morphology change, that negatively affects the further analysis and causes accidental damage to the membrane.

During the loading on the 2D membrane, bias voltage can be also applied to study the stress-dependent electrical properties. Upward and downward tests have been conducted. Although the boundary condition is changed in the upward test, valuable data can provide much information in electrical response of applying local strain onto the 2D membrane. Thus, the barrier height and width change with the stress. On the other hand, the results of downward test indicate the opposite trend for the electrical conductivity change with stress from upward test. Moreover, the potential barrier is independent of the stress, but the barrier width decreases with the stress. From this experiment, the preliminary

understanding of stress to electrical properties is found. However, the further experiments are recommended to conduct downward tests on the middle of a single-layered membrane which covers a whole grid of quantifoil. The stress applied would be more balanced and the theoretical calculation can be simplified.

4.5. *In Situ* Flexural Test

The flexural test describes the flexural properties of 2D membranes by analysing the morphology change with theoretical calculations (Details in **Publication 1**). To avoid being plagiarism and disturbing the process of publication, the contents can be briefly introduced here. Although AFM experiment can provide actual values of the force and morphology check, the continuous monitoring and 3-axes manipulations are absent. Therefore, TEM characterizations with *in situ* manipulations were employed to achieve real-time observations. During the manipulations, some wrinkles were formed on the 2D membranes and the shape of wrinkles has been theoretically modelled. The shape transition condition has been determined for both experimental and theoretical results. Moreover, the mechanisms of releasing strain of the wrinkles have been recognized due to the height of wrinkles. This flexural experiment is beneficial to the fundamental studies of nano-mechanics. If it is interested, it is recommended to read the publication. The contribution in this flexural test is to design an add-on for the *in situ* holder, discuss how to do the experiments together, and discuss the results and share our data.

Chapter 5. Conclusions

TEM characterizations with *in situ* mechanical and electrical manipulations on 2D materials have been conducted. Real-time monitoring on the structure-properties relation has provided valuable information for understanding the mechanism and properties of ultrathin membrane in electrical and mechanical properties. 2D electrical contacts and mechanical test have been demonstrated which successfully complete the objectives. These two categories will be concluded below.

Different from the bulk contacts, due to the reduced dimension in 2D materials, the current is mainly attributed to field emission through ultra-thin potential barriers. The forward and reverse behaviour are almost the same. The thickness and geometry dependent transport comes from the shifting of band states and different band alignments. The face contact is more easily influenced by the mid-gap defects states and Fermi level pinning effect, which will yield higher barriers for transport. The differences in vertical and in-plane screening in 2D materials also lead to different barrier widths. The current density-voltage plots in two contact geometry shows similar thickness dependence. The electrical conductivity has been compared in J-V plots, that indicates the conductivity increases with reducing the number of layers. There is another method to reduce the contact resistances, by introducing the screw dislocations into multilayer 2D contacts. It can be understood easily by a circuit diagram. Hence, according to the results, the edge contact with monolayer MoS_2 (or other 2D semiconductors) is the best contact which has the highest similarity with “Ohmic contact” and the IV responses least affected by contact issue. Although the I-V measurements are well reproducible in the same spot, errors caused by impurities and environmental fluctuations are unavoidable which affect the stability of the 2D contacts and hence the measurements. It is recommended to conduct

the experiment in the session with less environmental noise and freshly synthesized specimen. In the future, other 2D materials will be tested, especially for the materials with phase transformation.

The welding of WO_3 between W tip and multilayer MoS_2 has been observed for under 10.00 V bias voltage test. The I-V characteristic of the contact implies TFE is dominant. On the other hand, the Ag nanowire probe has been used to make a contact with multilayer MoS_2. The characteristic of Ag also creates an intimately contact which also behaves following TFE. The coincidence of these two M-S contacts implies the intimate M-S contact behaves like TFE.

The loading test in 2D Ti alloy has been conducted that indicates the grain boundary is the weakest overall. The strain will be released by cracking from along the grain boundary, if the bending of 2D Ti alloy is strong enough. The crystal planes of the grain boundary will be further analysed later. Moreover, in the stress-dependent test, the tunnelling current and barrier shape provide preliminary insight. The local stress would gradually change the conductivity and the formation of barrier. However, the changing mechanism is still under investigation.

In conclusions, TEM characterizations with *in situ* mechanical and electrical stimulations on 2D materials have significant implications that allows the direct observation of the structure-function relation. Based on the findings above, the results contribute to the fundamental understanding of 2D electrical contacts, dynamic properties and the mechanical properties as well as the mechanisms about releasing strain. This helps the prediction of the other 2D materials with similar structures. The findings are also beneficial to the next-generation electronic devices and other applications in design, processing and

manufacture. The most concern of 2D devices is about stability and feasibility. The related researches will keep investigations. Other than testing the other 2D materials in the same way to expend the sample size of the tunnelling barrier, phase transformation induced by either electricity or mechanical force are interested. In order to treat this problem, lower accelerating voltage TEM with Cs correction is recommended to minimize the effect by electron irradiation and record clearer structural change. Hopefully, other hidden properties and unknown mechanisms can be discovered by *in situ* manipulations in the future.

Reference

1. S. Iijima, J Cryst Growth **50** (3), 675-683 (1980).

2. E. A. Rohlfing, D. M. Cox and A. Kaldor, J Chem Phys **81** (7), 3322-3330 (1984).

3. S. Iijima, Nature **354** (6348), 56-58 (1991).

4. P. J. Goodhew, A. J. Clarke and J. E. Bailey, Materials Science and Engineering **17** (1), 3-30 (1975).

5. J. E. Hatch, A. Aluminum and M. American Society for, *Aluminum : properties and physical metallurgy*. (American Society for Metals, Metals Park, Ohio, 1998).

6. X. Huang, Materials **2** (4), 2369-2403 (2009).

7. I. Mohammed and A. R. Abu Talib, Advances in Materials and Processing Technologies **5** (1), 123-131 (2018).

8. T. Sinmazçelik, E. Avcu, M. Ö. Bora and O. Çoban, Materials & Design **32** (7), 3671-3685 (2011).

9. G. D. Lawcock, L. Ye, Y. W. Mai and C. T. Sun, Composites Science and Technology **57** (12), 1609-1619 (1998).

10. R. W. Keyes, IEEE Solid-State Circuits Society Newsletter **11** (3), 25-27 (2006).

11. K. S. Novoselov, A. K. Geim, S. V. Morozov, D. Jiang, Y. Zhang, S. V. Dubonos, I. V. Grigorieva and A. A. Firsov, Science **306** (5696), 666-669 (2004).

12. M. Xu, T. Liang, M. Shi and H. Chen, Chem Rev **113** (5), 3766-3798 (2013).

13. S. Z. Butler, S. M. Hollen, L. Cao, Y. Cui, J. A. Gupta, H. R. Gutierrez, T. F. Heinz, S. S. Hong, J. Huang, A. F. Ismach, E. Johnston-Halperin, M. Kuno, V. V. Plashnitsa, R. D. Robinson, R. S. Ruoff, S. Salahuddin, J. Shan, L. Shi, M. G. Spencer, M. Terrones, W. Windl and J. E. Goldberger, ACS Nano **7** (4), 2898-2926 (2013).

14. S. Das, J. A. Robinson, M. Dubey, H. Terrones and M. Terrones, Annu Rev Mater Res **45** (1), 1-27 (2015).

15. W. Choi, N. Choudhary, G. H. Han, J. Park, D. Akinwande and Y. H. Lee, Materials Today **20** (3), 116-130 (2017).

16. H. Y. Chang, M. N. Yogeesh, R. Ghosh, A. Rai, A. Sanne, S. Yang, N. Lu, S. K. Banerjee and D. Akinwande, Adv Mater **28** (9), 1818-1823 (2016).

17. R. Wei, H. Zhang, X. Tian, T. Qiao, Z. Hu, Z. Chen, X. He, Y. Yu and J. Qiu, Nanoscale **8** (14), 7704-7710 (2016).

18. Y. Yang, H. Fei, G. Ruan, C. Xiang and J. M. Tour, Adv Mater **26** (48), 8163-8168 (2014).

19. F. Crick, *What mad pursuit : a personal view of scientific discovery*. (1990).

20. D. B. Williams and C. B. Carter, *Transmission electron microscopy : a textbook for materials science. 3, 3*. (Plenum Press, New York, 2009).

21. J. Y. Huang, S. Chen, Z. Q. Wang, K. Kempa, Y. M. Wang, S. H. Jo, G. Chen, M. S. Dresselhaus and Z. F. Ren, Nature **439** (7074), 281 (2006).

22. Y. Lu, J. Y. Huang, C. Wang, S. Sun and J. Lou, Nature Nanotechnology **5**, 218 (2010).

23. C. Jin, K. Suenaga and S. Iijima, Nat Nanotechnol **3** (1), 17-21 (2008).

24. J. Zhao, H. Sun, S. Dai, Y. Wang and J. Zhu, Nano Lett **11** (11), 4647-4651 (2011).

25. J. Luo, Y. J. Xing, J. Zhu, D. P. Yu, Y. G. Zhao, L. Zhang, H. Fang, Z. P. Huang and J. Xu, Advanced Functional Materials **16** (8), 1081-1085 (2006).

26. Z. Y. Zhang, C. H. Jin, X. L. Liang, Q. Chen and L.-M. Peng, Applied Physics Letters **88** (7), 073102 (2006).

27. J. Y. Huang, L. Zhong, C. M. Wang, J. P. Sullivan, W. Xu, L. Q. Zhang, S. X. Mao, N. S. Hudak, X. H. Liu, A. Subramanian, H. Fan, L. Qi, A. Kushima and J. Li, Science **330** (6010), 1515-1520 (2010).

28. A. T. DeLaRiva, T. W. Hansen, S. R. Challa and A. K. Datye, Journal of Catalysis **308**, 291-305 (2013).

29. Y. Zhu, M. Q. Xu and W. Zhou, Chinese Physics B **27** (5), 056804 (2018).

30. K. Kamatani, K. Higuchi, Y. Yamamoto, S. Arai, N. Tanaka and M. Ogura, Scientific Reports **5**, 10161 (2015).

31. X. Liu, J. D. Wood, K. S. Chen, E. Cho and M. C. Hersam, J Phys Chem Lett **6** (5), 773-778 (2015).

32. J. Y. Huang, F. Ding, B. I. Yakobson, P. Lu, L. Qi and J. Li, Proc Natl Acad Sci U S A **106** (25), 10103-10108 (2009).

33. V. Teodorescu, L. Nistor, H. Bender, A. Steegen, A. Lauwers, K. Maex and J. Van Landuyt, Journal of Applied Physics **90** (1), 167-174 (2001).

34. M. Humphrey, P. V. Pancella and N. Berrah, (2015).

35. R. F. Egerton, P. Li and M. Malac, Micron **35** (6), 399-409 (2004).

36. R. F. Egerton, Microsc Res Tech **75** (11), 1550-1556 (2012).

37. D. Bouscaud, R. Pesci, S. Berveiller and E. Patoor, Ultramicroscopy **115**, 115-119 (2012).

38. F. Hosokawa, H. Sawada, Y. Kondo, K. Takayanagi and K. Suenaga, Microscopy (Oxf) **62** (1), 23-41 (2013).

39. J. Zhao, Q. M. Deng, T. H. Ly, G. H. Han, G. Sandeep and M. H. Rummeli, Nature Communications **6**, 8935 (2015).

40. K. S. Kim, Y. Zhao, H. Jang, S. Y. Lee, J. M. Kim, K. S. Kim, J. H. Ahn, P. Kim, J. Y. Choi and B. H. Hong, Nature **457** (7230), 706-710 (2009).

41. X. Li, F. Zhang and Q. Niu, Phys Rev Lett **110** (6), 066803 (2013).

42. W. Wu, L. Wang, Y. Li, F. Zhang, L. Lin, S. Niu, D. Chenet, X. Zhang, Y. Hao, T. F. Heinz, J. Hone and Z. L. Wang, Nature **514** (7523), 470-474 (2014).

43. H. Zhu, Y. Wang, J. Xiao, M. Liu, S. Xiong, Z. J. Wong, Z. Ye, Y. Ye, X. Yin and X. Zhang, Nature Nanotechnology **10**, 151 (2014).

44. D. Costanzo, S. Jo, H. Berger and A. F. Morpurgo, Nat Nanotechnol **11** (4), 339-344 (2016).

45. N. Choudhary, M. Patel, Y. H. Ho, N. B. Dahotre, W. Lee, J. Y. Hwang and W. Choi, Journal of Materials Chemistry A **3** (47), 24049-24054 (2015).

46. L. David, R. Bhandavat and G. Singh, ACS Nano **8** (2), 1759-1770 (2014).

47. Y. Niu, R. G. Wang, W. C. Jiao, G. M. Ding, L. F. Hao, F. Yang and X. D. He, Carbon **95**, 34-41 (2015).

48. S. Lin, X. Li, P. Wang, Z. Xu, S. Zhang, H. Zhong, Z. Wu, W. Xu and H. Chen, Sci Rep **5**, 15103 (2015).

49. Y. K. Srivastava, A. Chaturvedi, M. Manjappa, A. Kumar, G. Dayal, C. Kloc and R. Singh, Advanced Optical Materials **5** (23), 1700762 (2017).

50. A. Dankert and S. P. Dash, Nature Communications **8**, 16093 (2017).

51. S. Yu, Q. Rice, B. Tabibi, Q. Li and F. J. Seo, Nanoscale **10** (26), 12472-12479 (2018).

52. S. Dai, J. Zhao, L. Xie, Y. Cai, N. Wang and J. Zhu, Nano Letters **12** (5), 2379-2385 (2012).

53. C. Jin, H. Lan, L. Peng, K. Suenaga and S. Iijima, Physical Review Letters **102** (20), 205501 (2009).

54. S. Cho, S. Kim, J. H. Kim, J. Zhao, J. Seok, D. H. Keum, J. Baik, D. H. Choe, K. J. Chang, K. Suenaga, S. W. Kim, Y. H. Lee and H. Yang, Science **349** (6248), 625-628 (2015).

55. F. J. Urbanos, A. Black, R. Bernardo-Gavito, A. L. Vazquez de Parga, R. Miranda and D. Granados, Nanoscale **11** (23), 11152-11158 (2019).

56. A. Allain, J. Kang, K. Banerjee and A. Kis, Nat Mater **14** (12), 1195-1205 (2015).

57. Y. Liu, N. O. Weiss, X. D. Duan, H. C. Cheng, Y. Huang and X. F. Duan, Nature Reviews Materials **1** (9), 16042 (2016).

58. D. S. Schulman, A. J. Arnold and S. Das, Chem Soc Rev **47** (9), 3037-3058 (2018).

59. D. F. Brailsford and A. J. B. Robertson, International Journal of Mass Spectrometry and Ion Physics **1** (1), 75-85 (1968).

60. P. Poncharal, Z. L. Wang, D. Ugarte and W. A. de Heer, Science **283** (5407), 1513-1516 (1999).

61. C. Q. Chen, Y. Shi, Y. S. Zhang, J. Zhu and Y. J. Yan, Phys Rev Lett **96** (7), 075505 (2006).

62. R. B. Gennis, *Biomembranes : molecular structure and function*. (Springer, [Place of publication not identified], 2014).

63. S. R. Gillmer, D. Z. Fang, S. E. Wayson, J. D. Winans, N. Abdolrahim, J. P. S. DesOrmeaux, J. Getpreecharsawas, J. D. Ellis, P. M. Fauchet and J. L. McGrath, Thin Solid Films **631**, 152-160 (2017).

64. H. Clausen-Schaumann, M. Seitz, R. Krautbauer and H. E. Gaub, Curr Opin Chem Biol **4** (5), 524-530 (2000).

65. K. S. Novoselov, V. I. Fal'ko, L. Colombo, P. R. Gellert, M. G. Schwab and K. Kim, Nature **490** (7419), 192-200 (2012).

66. K. F. Mak, C. Lee, J. Hone, J. Shan and T. F. Heinz, Phys Rev Lett **105** (13), 136805 (2010).

67. Y. Wei, B. Wang, J. Wu, R. Yang and M. L. Dunn, Nano Lett **13** (1), 26-30 (2013).

68. C. Lee, X. Wei, J. W. Kysar and J. Hone, Science **321** (5887), 385-388 (2008).

69. G. Seifert, H. Terrones, M. Terrones, G. Jungnickel and T. Frauenheim, Phys Rev Lett **85** (1), 146-149 (2000).

70. L. C. Qin, X. Zhao, K. Hirahara, Y. Miyamoto, Y. Ando and S. Iijima, Nature **408** (6808), 50 (2000).

71. L. Ortolani, E. Cadelano, G. P. Veronese, C. D. Boschi, E. Snoeck, L. Colombo and V. Morandi, Nano Lett **12** (10), 5207-5212 (2012).

72. S. Wayne Cranford and M. J. Buehler, (2012).

73. S. Bhattacharya and K. P. Ghatak, *Fowler-Nordheim Field Emission Effects in Semiconductor Nanostructures*. (Springer Berlin, Berlin, 2014).

74. S. M. Sze, *PHYSICS OF SEMICONDUCTOR DEVICES*. (JOHN WILEY, [Place of publication not identified], 2019).

75. O. L. Guise, J. W. Ahner, M. C. Jung, P. C. Goughnour and J. T. Yates, Nano Letters **2** (3), 191-193 (2002).

76. M. J. Manfra, Annu Rev Conden Ma P **5** (1), 347-373 (2014).

77. A. Özden, F. Ay, C. Sevik and N. K. Perkgöz, Japanese Journal of Applied Physics **56** (6S1), 06GG05 (2017).

78. Z. Lin, Y. Zhao, C. Zhou, R. Zhong, X. Wang, Y. H. Tsang and Y. Chai, Scientific Reports **5**, 18596 (2015).

79. I. Bilgin, F. Liu, A. Vargas, A. Winchester, M. K. Man, M. Upmanyu, K. M. Dani, G. Gupta, S. Talapatra, A. D. Mohite and S. Kar, ACS Nano **9** (9), 8822-8832 (2015).

80. D. Zhou, H. Shu, C. Hu, L. Jiang, P. Liang and X. Chen, Crystal Growth & Design **18** (2), 1012-1019 (2018).

81. J.-i. Fujita, T. Hiyama, A. Hirukawa, T. Kondo, J. Nakamura, S.-i. Ito, R. Araki, Y. Ito, M. Takeguchi and W. W. Pai, Scientific Reports **7** (1), 12371 (2017).

82. L. Jiao, H. J. Liu, J. L. Chen, Y. Yi, W. G. Chen, Y. Cai, J. N. Wang, X. Q. Dai, N. Wang, W. K. Ho and M. H. Xie, New Journal of Physics **17** (5), 053023 (2015).

83. N. Hanada, T. Ichikawa and H. Fujii, Journal of Alloys and Compounds **404**, 716-719 (2005).

84. T. Xing, S. Mateti, L. H. Li, F. Ma, A. Du, Y. Gogotsi and Y. Chen, Sci Rep **6**, 35532 (2016).

85. J. N. Coleman, M. Lotya, A. O'Neill, S. D. Bergin, P. J. King, U. Khan, K. Young, A. Gaucher, S. De, R. J. Smith, I. V. Shvets, S. K. Arora, G. Stanton, H. Y. Kim, K. Lee, G. T. Kim, G. S. Duesberg, T. Hallam, J. J. Boland, J. J. Wang, J. F. Donegan, J. C. Grunlan, G. Moriarty, A. Shmeliov, R. J. Nicholls, J. M. Perkins, E. M. Grieveson, K. Theuwissen, D. W. McComb, P. D. Nellist and V. Nicolosi, Science **331** (6017), 568-571 (2011).

86. V. Nicolosi, M. Chhowalla, M. G. Kanatzidis, M. S. Strano and J. N. Coleman, Science **340** (6139), 1420-+ (2013).

87. J. J. Wu, M. J. Liu, K. Chatterjee, K. P. Hackenberg, J. F. Shen, X. L. Zou, Y. Yan, J. Gu, Y. C. Yang, J. Lou and P. M. Ajayan, Advanced Materials Interfaces **3** (9), 1500669 (2016).

88. C. Backes, T. M. Higgins, A. Kelly, C. Boland, A. Harvey, D. Hanlon and J. N. Coleman, Chemistry of Materials **29** (1), 243-255 (2017).

89. J. D. Caldwell, T. J. Anderson, J. C. Culbertson, G. G. Jernigan, K. D. Hobart, F. J. Kub, M. J. Tadjer, J. L. Tedesco, J. K. Hite, M. A. Mastro, R. L. Myers-Ward, C. R. Eddy, P. M. Campbell and D. K. Gaskill, ACS Nano **4** (2), 1108-1114 (2010).

90. J. M. Cowley, in *Diffraction Physics (Third Edition)*, edited by J. M. Cowley (North-Holland, Amsterdam, 1995), pp. 231-254.

91. A. Kumar and P. K. Ahluwalia, The European Physical Journal B **85** (6), 186 (2012).

92. C. Gong, H. J. Zhang, W. H. Wang, L. Colombo, R. M. Wallace and K. J. Cho, Applied Physics Letters **103** (5), 053513 (2013).

93. S. Choi, Z. Shaolin and W. Yang, Journal of the Korean Physical Society **64** (10), 1550-1555 (2014).

94. R. G. Forbes, J. H. B. Deane, A. Fischer and M. S. Mousa, Jordan Journal of Physics **8** (3), 125-147 (2015).

95. M. Reiche, M. Kittler, W. Erfurth, E. Pippel, K. Sklarek, H. Blumtritt, A. Haehnel and H. Uebensee, Journal of Applied Physics **115** (19), 194303 (2014).

96. B. S. Simpkins, E. T. Yu, P. Waltereit and J. S. Speck, Journal of Applied Physics **94** (3), 1448-1453 (2003).

97. V. H. Babu, U. V. Subba Rao and K. Venkata Ramiah, Physica Status Solidi (a) **28** (1), 269-277 (1975).

98. Y. Ishikawa, K. Yamauchi, C. Yamamoto and M. Tabe, Mater Res Soc Symp P **864**, 253-258 (2005).

99. S. J. Lee, Y. H. Kim, J. K. Kim, H. Baik, J. H. Park, J. Lee, J. Nam, J. H. Park, T. W. Lee, G. R. Yi and J. H. Cho, Nanoscale **6** (20), 11828-11834 (2014).

100. H. Jang, C. R. Ryder, J. D. Wood, M. C. Hersam and D. G. Cahill, Adv Mater **29** (35), 1700650 (2017).

101. X. K. Gu, B. W. Li and R. G. Yang, Journal of Applied Physics **119** (8), 085106 (2016).